Master Thesis

Doping Layers in Quantum Cascade Lasers:

A study in doping density, position and migration effects.

Josefin Reftlér

Supervised by: Andreas Wacker
Division of Mathematical Physics, Lund University

Thesis presented: April 8, 2015

Abstract

Quantum Cascade Lasers (QCLs) consist of several semiconductor materials sandwiched together. The QCL achieves stimulated emission in the mid-IR (m-IR) to the THz region of the electromagnetic spectrum by inter-subband transitions. These parts of the electromagnetic spectrum are hard to lase in with conventional means. This makes them highly eligible in spectroscopic applications used in many research areas including chemistry, physics and medicine. These structures are also important because instead of a large laser which requires much equipment to lase in the wanted region, only a small chip can be used. The QCLs which lase in the IR operate at room temperature, but the operating temperature of the THz QCLs is low which constitutes a problem. This limits their applicability. It is therefore beneficial to have a THz system which operates at room temperature. Hence continued research about these systems (in the THz) is important.

In this thesis work, three studies have been performed. The first study investigated the impact of changing the doping density. The second study considered the impact of changing the position of the doping layer. The third study investigated if dopant migration effects can account for experimental results on symmetric QCLs. This thesis work is theoretical and the results are simulated using a FORTRAN programme which is based on Non Equilibrium Green's Function Theory (NEGFT). The results of the studies will be compared to experimental measurements when this is possible.

In this investigation it has been shown that the current densities and the gain are highly dependent on the doping density and the position of the doping layer. Dopant migration effects have also been investigated and it has been found that the case when the diffusion of the charge carriers have spread out over almost the entire period gives the closest correspondence to the reference results.

Acknowledgements

I want to thank my supervisor Andreas Wacker and his research group for the opportunity to work with this subject. Also for the great opportunity to participate in the International Quantum Cascade Laser School and Workshop 2014, IQCLSW2014. Thanks to David Winge and Martin Franckié for taking time to answer my questions. Finally thanks to Kasparas Krivas who made poster work with me for IQCLSW2014.

List of Abbreviations

- QCL: Quantum Cascade Laser.
- m-IR: Mid Infra Red.
- THz: Tera (10^{12}) Hertz (1/s).
- K: Kelvin, SI-unit of temperature.
- ULS: Upper Laser State, see section 2.1
- LLS: Lower Laser State, see section 2.1
- CB: Conduction Band, see section 2.1
- SF : Static Field, see section 3.2.
- Scatt: Short for scattering.
- AC: ac-field, see section 3.2.2.
- IFR: Interface Roughness Scattering, see section 3.3.
- I-V plot: Current Density versus Bias per period, see sections 7,8,9.
- NDR: Negative Differential Resistance, it is defined

$$\Delta R = \frac{\Delta V}{\Delta I} < 0\,.$$

- MF: Mean Field potential, see section 3.2.3
- Planck's constant $h = 6.626 \cdot 10^{-34}$ unit Js.
- Frequency f unit s^{-1}.

Contents

1 Introduction

The Quantum Cascade Laser (QCL) [1] is a semiconductor device which emits radiation in the IR and THz region of the electromagnetic spectrum. [2] In large parts of the IR, between 3.4-24 μm [3], these devices reach operating temperatures as high as 300 K, which makes them eligible in spectroscopic applications ranging from medicine to chemistry [4]; however in the THz region these devices have limited operating temperatures, with the current temperature record around 200 K [5]. This limits the practical applications of the THz QCL. Thus improving these devices is of technical importance and requires a deep understanding of how the QCL performance depends on the semiconductor structure. Here the doping profile and density are two important attributes as these enables the current flow through the device. This thesis aims to quantify how these two attributes affect the performance of the QCL.

Quantum Cascade Lasers

The QCL was first demonstrated in 1994 by Frederico Capasso and his research group at Bell laboratories [1, 6]. The QCL is constructed by sandwiching different semiconductor materials, typically III,V materials, e.g GaAs/$Al_xGa_{1-x}As$ and InGaAs/$Al_xIn_{1-x}As$ [3], together. These materials have different band gaps, so when assembling these materials it will result in an energy offset in the conduction band. This creates a structure of consecutive wells and barriers (see figure 1). Discrete states arise which will not be localised to only one well, but rather to the period of wells and barriers. This is depicted in figure 1. The period is repeated N times during the growth of the laser.

At the operating bias the electron will tunnel through the barrier at the start of the period and through a state called the injector state (plotted in blue in figure 1) end up in the Upper Laser State (ULS, plotted in green in figure 1) of the period. If the system is affected by an optical field, the electron will transit down to the Lower Laser State (LLS, plotted in red in figure 1) emitting a photon in the process. Then the electron is extracted from the LLS (in figure 1 via the emission of an optical phonon) and injected into the next period by the injector state by resonant tunnelling. The extraction process depends on the semiconductor material (height of barrier and widths of wells and barriers). These structures can be grown using a variety of techniques, two of which are molecular beam epitaxy (MBE) and metalorganic vapor phase epitaxy (MOVCD) [7]. A limitation with any of these processes is that the doping density cannot be determined exactly, only estimated [8] which has to be considered when comparing the calculated to experimental results.

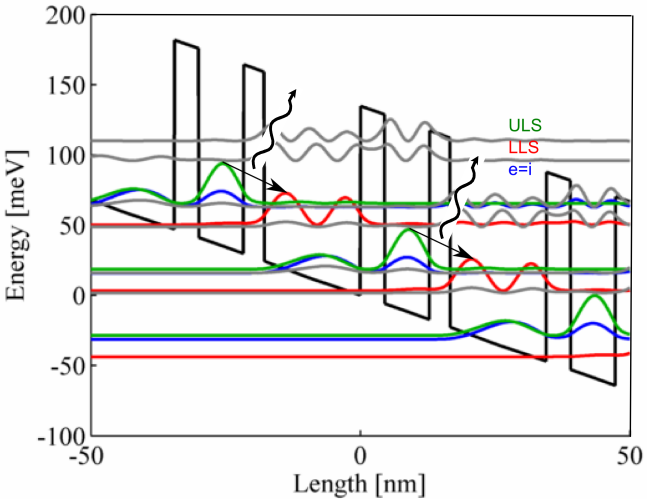

Figure 1: A simple two well two barrier structure (see reference [9]). The conduction band edge (black) and the probability densities for the relevant quantum states (in color) are plotted. Three periods have been plotted. The green state is the ULS, the red is the LLS, and the blue state here is the extraction and injector state. The photon energy is $E = hf = E_{ULS} - E_{LLS}$, h is Planck's constant and f is the frequency.

Motivation

The aim of this thesis can be enunciated in a couple of questions. These will be answered by investigating the impact that changing the doping position and density has on the current densities and the gain of the QCLs. The main questions are the following.

- What is the effect of changing the doping density of the sample?
- How important is the position of the charge carriers, i.e what happens when the position of the doping changes?
- Can dopant migration effects be simulated and will these affect the output of the laser?

Dopant Migration means that the added impurities will diffuse through out the structure when the layers are grown, and the doping profile will end up being an other than the predicted one. That is why the predicted (nominal) doping profile will be compared to a migrated profile and see if the migratory effects can account for the experimental results in reference [10]. This work will be theoretical and the results are modelled using a model based on Non Equilibrium Greens Function Theory (NEGFT) [2].

Summary of Results

In the scope of this investigation it has been shown that while keeping the sizes of the wells and barriers constant and changing the doping layer only by moving it or changing the doping density will affect the I-V curves and the gain considerably. Thus the same periodic structure can be made to lase differently just by changing the doping layers position and/or by increasing the number of charge carriers. Also it has been found that dopant migration effects will affect the output of the laser if the migration effects are large; the worst case scenario of the doping migration (see figure 17 (b) profile (4) presented in section 9.7). Some care has to be taken when interpreting the results as the model does not contain all the possible scattering mechanisms in the sample. It lacks the electron-electron scattering and will account for some of the discrepancies between the calculated I-V plots and gain compared to the experimental results.

Part I
Theory

2 Quantum Cascade Lasers

Quantum cascade lasers (QCLs) are constructed by *super-lattices*. These super-lattices consist of a series of different semiconductor materials which are periodically arranged. Each one of these super-lattices is constituted by a *heterostructure* (an alloy of semiconductor materials). The conduction band edge of this heterostructure forms a series of wells and barriers because the materials have different band-gaps (different energy dispersion). The wells and barriers which are non repetitive constitute one period which is then repeated N times during the growth of the system. In the quantum wells discrete states in z (but plane waves in xy) arise and these are described by the Schrödinger equation using the effective Hamiltonian. (The programme does not solve the Schrödinger equation but solves the Dyson and Keldysh equations, see section 4). The discrete states will form subbands in the conduction band; an example of these subbands can be found in figure 1. These subbands are utilised as light is emitted during a transition from one of the higher subbands to the lower subband. [3,6] This process can be seen in figure 1, where the arrows indicates the states involved. The best case scenario is when only one photon energy is received, i.e the optical transition only occurs between the Upper Laser State (ULS) to the Lower Laser State (LLS). Often the optical transition occurs from several of the higher states to the lower. This depends on the structure of the QCLs.

First the concepts of the QCL will be dealt with, in an easy at hand approach following the outline of reference [6]. Then the programme used to calculate the *I-V* and gain characteristics, which is based on the *Non Equilibirum Green's Function Theory* (NEGFT), will be discussed shortly based on the theory in reference [2].

2.1 Laser Design

As indicated by its name, as hetero means different, a heterostructure consists of slices of different semiconductor materials, which construct the QCL. These slices form one crystal which will have the same lattice constant, but will have different intrinsic carrier densities around the boundary between the materials. Common semiconductor materials used are GaAs and $Al_xGa_{1-x}As$ (x is the relative amount of aluminium to gallium). Other types of semiconductor materials are $Al_xIn_{1-x}As$/InGaAs and $Ga_xIn_{1-x}As/Al_xIn_{1-x}As$/InP [4, 11]. This thesis will concentrate on laser structures based on GaAs/$Al_xGa_{1-x}As$.

The different materials that are assembled have different energy dispersion. When these materials are put together the bands will bend accordingly and create an energy offset in the bands. The energy offset Δ depends on the materials and on the relative composition of the well and barrier materials. The energy offset will be in the order of magnitude of hundreds of meV. This offset can be seen in figure 2,

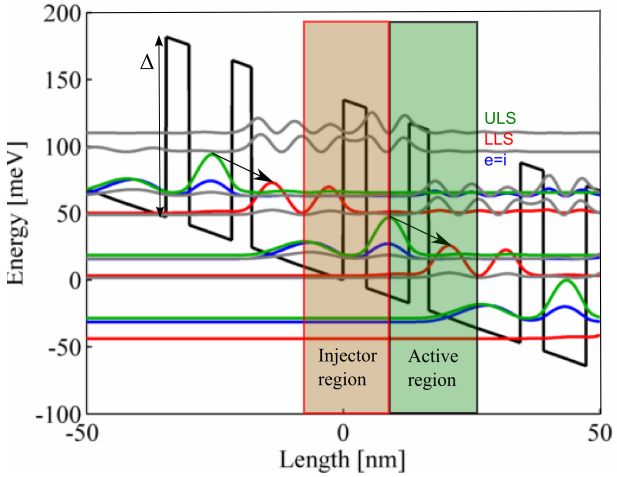

Figure 2: The probability density plotted at a bias of 47mV per period, for the first five bands of the two well laser [9]. Here the active and injector regions of the laser can be seen. The energy offset Δ is the energy height of the barrier. The arrows indicate between which states the laser transition occurs.

where the conduction band and the band structure are plotted. Cascade means a flow or fall in large quantities and this occurs in these laser structures as one single electron has the possibility of emitting one photon per period throughout the entire structure during the transition from a higher energy state to a lower one. [2, 3, 6]

The QCL is divided into the *injector* and the *active* region, see figure 2. The purpose of the injector region is to raise the energy of the electrons and place them in the ULS. The injector region is the red region in figure 2 and the ULS is plotted in green. In the active region the laser transition occurs and the electron is placed in the LLS. This occurs in the green part of figure 2. The extraction from the lower laser state is also a process which takes place in the active region. The extraction states' purpose is to efficiently deplete the LLS of electrons, so efficient *inversion* occurs, otherwise there will be no gain. Inversion means that the population of charge carriers in the LLS is lower than in the ULS and is defined $\Delta n = n_{ULS} - n_{LLS}$. Hence the extraction process is important. [12] How this is achieved depends on the design of the laser. The efficiency of these processes, depends on the lifetimes of the states, these in turn depends on the laser design. If the extraction process is too slow, the inversion is inhibited. [6, 12, 13]

So what is important to think about when making a laser? One wants a high enough oscillator strength, which is a measure on how strong the laser transition is. In reference [6] page 57 this is defined

$$f_{\nu'\nu} = \frac{2m}{\hbar^2}|z_{\nu'\nu}|^2(E_\nu - E_{\nu'})$$

where $z_{\nu'\nu}$ is the dipole matrix element, and E_ν and $E_{\nu'}$ are the energies of the

states before and after the transition. The dipole matrix element depends on the overlap of the wave-functions and the energy difference between the states. When constructing the laser it is also important to consider that there always will be intrinsic broadening of the states. If the energy levels are separated by less energy than this broadening, then the occupation will be shared by many states. This translates to that the scattering rate decreases because the rate is shared by the states. [6] The QCL is often designed to take advantage of the materials longitudinal optical phonon to extract the charge carriers from the LLS or from the extraction state. The longitudinal optical phonon frequency and hence the extraction energy in turn depends on the material. That is why it is important to use materials which have the same lattice constant when constructing the laser. [6, 8]

The limitations of the QCL depend on a number of parameters. One is the longitudinal phonon energy of the semiconductor material as photons near this energy cannot propagate through the crystal - this is called the reststrahlen effect. [6] [13] Another is the temperature because if the temperature matches the energy difference between the extraction level and the LLS the electrons can be placed back into the LLS, a behaviour called thermal backfilling. Also the higher the temperature is the higher the escape current will be as the electron will be thermally excited to higher energy bands which are not participating in the lasing event. [6]

3 The Model Hamiltonian

3.1 Basis States

The wavefunctions used to describe crystal structures are usually based on the so called *Bloch* functions: [14, 15]

$$\varphi^{\nu}_{\mathbf{k}}(\mathbf{r}) = e^{i\mathbf{k}\cdot\mathbf{r}} u^{\nu}_{\mathbf{k}}(\mathbf{r}) \ , \tag{1}$$

where $\mathbf{k}$ is the Bloch vector, ν is the subband index and $u^{\nu}_{\mathbf{k}}(\mathbf{r})$ contains the periodicity of the lattice. [13, 14] The notation for the quantum states will in the rest of this thesis be denoted $\alpha = (n, \nu)$, where n is the period and ν denotes the subband. As these Bloch functions are highly de-localised, they are not suitable to describe the kinetics of the QCL. The Bloch functions do however provide a complete set of basis states for the Hamiltonian describing these types of crystal structures giving a good starting point. [2, 13] Starting with the Bloch functions, and summing them over the possible k-values up to an arbitrary phase

$$\psi^{\nu}_{\mathbf{R}} = \frac{1}{\sqrt{N}} \sum_{\mathbf{k}} e^{-i\mathbf{k}\cdot\mathbf{R}} \varphi^{\nu}_{\mathbf{k}}(\mathbf{r}) \ , \tag{2}$$

where $\mathbf{R}$ is an arbitrary lattice vector and N is the number of unit cells, gives the states which describe the dynamics of the system. These states are called *Wannier* states. The Wannier states in the model are defined in the growth (z) - direction only as the crystal is symmetric and homogeneous in the xy-plan. $\vec{r}$ is then defined in periods of $(z - nd)$. [13] (More about this can be read in references [16] and [13].) When applying a bias to the modelled system, the discrete states will shift in response to the electric field. The model Hamiltonian will in this case have non-diagonal elements between the subbands ν. The Wannier states then shift and new states have to be calculated. The energy eigenstates will be given by the so - called *Wannier-Stark states*. [2, 13, 16] In the absence of an applied bias the Wannier functions describe the system. These Wannier functions are used in the implementation of the model. The Wannier-Stark states are in contrast only used when interpreting the results. The probability densities plotted in figures 1-2 are in Wannier-Stark basis. [2]

3.2 Hamiltonian

The Hamiltonian used in the model (describing the interactions taking place) is [2]

$$H = H_0 + H_{ac}(t) + H_{MF}(t) + H_{scatt} \, . \tag{3}$$

Here H_0 is the single particle Hamiltonian, which contains the heterostructure potential and kinetic energy. These are one-particle energies and static potentials. The second part of the Hamiltonian describes the optical field which induces laser transitions and the third part is the time dependent mean-field. This third part is created by the charge distribution in the heterostructure (the solution to Poisson's equation). H_{scatt} accounts for the scattering events that can take place. [2, 6] The Hamiltonian is expressed in second quantisation.

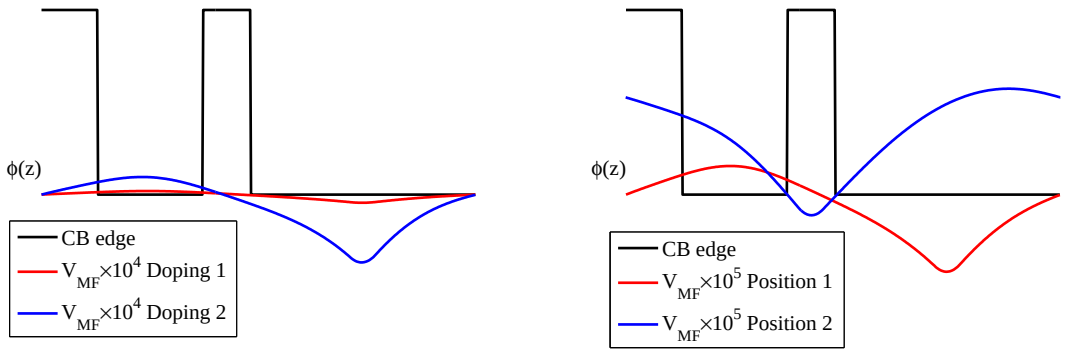

(a) (b)

Figure 3: The conduction band edge is plotted without at F=0 for the two well laser [9]. (a) The V_{MF} plotted at different doping densities. (b) The V_{MF} at different positions.

3.2.1 The Single Particle Hamiltonian

The single particle Hamiltonian contains three parts: the kinetic energy and the heterostructure potential T, the static electric field V_{SF} and the static part of the mean-field V_{MF}. The first contribution of the Hamiltonian can be expressed as

$$H_0 = T + V_{SF} + V_{MF} = \sum_{\alpha,\beta,\vec{k}} \left(T_{\alpha,\beta} + U^{SF}_{\alpha,\beta} + U^{MF}_{\alpha,\beta}\right) a^{\dagger}_{\beta}(\vec{k}) a_{\alpha}(\vec{k}) \ , \tag{4}$$

where α and β are indices which denote the quantum state before and after an event. So $\alpha = (n, \nu)$ where n is the period and ν is the energy level within that period n. Hence $\beta = (n', \nu')$ is the other state. [17] How this Hamiltonian is implemented is explained in [2].

3.2.2 The Optical Field

The optical field is expressed

$$H_{ac} = \sum_{\alpha\beta,\vec{k}} a^{\dagger}_{\beta}(\vec{k}) U^{AC}_{\alpha\beta}(t) a_{\alpha}(\vec{k}) \, . \tag{5}$$

[2, 12] which is used in order to calculate the gain.

3.2.3 The Mean Field Potential

The mean field potential V_{MF} (will for future reference be called the MF) is obtained from the solution to Poisson's equation

$$\nabla^2 \phi(z) = -\frac{\rho_{el}(z) + \rho_{dop}(z)}{\epsilon_0} \, . \tag{6}$$

The solution has to obey the boundary condition $\phi(z) = \phi(z+d)$. ρ_{el} is the electron charge density and ρ_{dop} is the impurity charge density. ρ_{el} will be the sum of the

intrinsic carrier density and the number of ionised impurity states. The MF will contain a static part and an oscillating part (time-dependent), due to the presence of the optical field. The behaviour of the MF can be seen in figure 3 where the impact of changing the doping (a) and the position (b) can be seen. The MF changes when the doping density $\rho_{dop}(z)$ changes, which is seen in figure 3(a) where the MFs for two doping densities can be seen. There will be a slight shift in energies due to this, however this will only be in the order of magnitude of 10^{-3}meV. [2] It will also be highly dependent on where the doping layer has been placed which can be seen in in figure 3(b) where the change is larger however still in the same order of magnitude. This is one of the parts of the Hamiltonian which will change when changing the doping layer.

3.3 The Scattering

Scattering is an important process which fills and depletes the states. These events are either inelastic (electron-phonon) or elastic (electron-electron, electron-impurity, and electron-interface). Scattering affects the inversion of the states and how effective the tunnelling is. First the different types of scattering will be shortly explained following the approach used in reference [6]. After that some of the mathematical implementations from reference [2] will be stated and discussed in order to provide a good overview of the different parameters which are important for the interpretation of the results.

Phonon scattering. *Phonons* are virtual particles which arise when the lattice vibrates. They carry the momentum and energy of the vibration. There are two types of phonons, *acoustical* and *optical*, the difference being the dispersion patterns. There will be a small polarisation potential where the lattice vibrates. This potential will interact with the electrons as they pass through the structure and hence scatter them [6, 14, 18]. Energy and momentum will be transferred to or from the lattice by the absorption or emission of phonons. [6] This rate will be set and will not change in the model.

Impurity scattering occurs when the electron scatters against the ionised donor states of the doping atoms. To investigate the impact of these events, the doping density and the position of the doping layer of the QCL will be changed. At low doping densities it can be argued that the contribution to the scattering matrix will be equally large as the other scattering mechanisms [6]. When increasing the doping the impurity density will become larger and more dominant. In research presented in reference [19], it was found that the scattering rate becomes significant at higher doping levels. So for low-doped materials the impurity scattering occurs, but becomes one of the dominant scattering mechanisms only at higher doping levels. [6].

Alloy scattering. The QCL is constructed by using alloys of different semiconductor materials. This alloy disorder destroys the translational invariance in the x-y plane of the potential and cause scattering due to this potential change. It is taken into account in the scattering matrix elements in the programme. It remains

constant as the relative amount will be the same in all the calculations. [2,6,12].

Interface roughness scattering(IFR) is due to the fact that the contact between the materials at the interface is not smooth, but has irregularities. These irregularities form regions of different semiconductor materials of dimensions (λ, η). These regions will have different potentials which will interact differently with the electrons when they pass through the structure and scatter them. This will not be investigated in this thesis and is independent of the doping density. It will be present, however constant. The interested reader can see the work presented in [2,12,13] and the thesis project performed by Kasparas Krivas.

Electron-electron scattering occurs when the electrons interact and exchange energy and momentum. The model does not take the electron-electron scattering into account, so the results have to be taken with a grain of salt. However when increasing the doping density the number of electron-electron scattering events would increase. For lower doping densities it can be argued that this will not affect the result much, but for higher doping densities this will give a larger deviation between the theoretical and experimental results. [2,6]

Spontaneous emission occurs when a discrete state de-excites from the ULS to the LLS by emitting a photon. This is a very slow process, having a very long lifetime. Hence it is far from the dominant mechanism. [6]

Stimulated emission is the process when a discrete state electron de-excites from the ULS to the LLS by emitting a photon. This is only possible when there is an optical field present as the optical matrix element has to be non-zero (i.e there has to be some initial spontaneous emission). The rate of the emission will depend on the oscillator strength $f_{\nu\nu'}$ between the two states ν and ν' and the energy of the transition $E_{\nu\nu'}$ and the strength of the optic field. This is used in the programme so it is essential to turn it on. This is also done in the input file to the NEGFT programme. More about how the programme works can be read in section 4. [2,6]

3.3.1 Impurity Scattering.

The tensor $X_{\alpha\alpha',\beta\beta'}$ is the angle averaged part of the scattering matrix element used in the calculation of the self-energies. This tensor is defined according to references [2] and [17]

$$X_{\alpha\alpha',\beta\beta'}(E_k, E_{k'}) = \frac{A}{(2\pi)^2}\frac{m*}{\hbar} \times \int_0^{2\pi} d\phi \langle V_{\alpha\beta}(E_k, E_{k'}, \phi) V_{\alpha'\beta'}(E_k, E_{k'}, \phi)\rangle \qquad (7)$$

where A is the area, m^* is the effective mass, $\phi \angle \mathbf{k}, \mathbf{k}'$ (i.e the angle between k-vectors before and after scattering) and the V's are the potentials. This is used in the calculation of the self-energy. The interested reader can find more about the self-energy and its implementation in references [2,17].

Investigating the impurity scattering only, the impurity part of the second rank tensor $X^{imp}_{\alpha\alpha,\beta\beta'}$ is changed. This tensor is defined according to reference [2]

$$\begin{aligned} X^{imp}_{\alpha\alpha'\beta\beta'}(E_k, E_{k'}) = &\sum_i N^i_{2D} \frac{e^2}{16\pi\epsilon_0^2\epsilon_s^2} \frac{1}{2\pi} \int_0^{2\pi} d\phi \\ &\times \left\{ \frac{1}{E_k + E_{k'} - 2\sqrt{E_k E_{k'}}\cos\phi + E_\lambda} \right\} \\ &\times \int dz_1 \phi^*_\alpha(z_1)\phi_\beta(z_1) e^{-q(\phi)|z_1 - z_i|} \\ &\times \int dz_2 \phi^*_{\beta'}(z_2)\phi_{\alpha'}(z_2) e^{-q(\phi)|z_2 - z_i|} \,. \end{aligned} \tag{8}$$

It can be seen in equation (8) that the impurity scattering depends on the doping density N_{2D} of each layer i, the dispersion energies before and after scattering as the overlap of the wave-functions. The scattering is treated in the programme as scattering from a number of δ-functions at position z_i and areal density N^i_{2D} instead of a homogeneous layer. The δ-function describes the presence of a layer where the impurities are placed, and gives scattering potentials treated as delta-like. In reference [2] this is explained by how the tensor $X_{\alpha\alpha',\beta\beta'}(E_k, E'_k)$ is approximated by the tensor $X_{\alpha\alpha',\beta\beta'}(E_{typ}, E_{typ'})$ in the computer code. [2, 13]

Using that $\tau_{scatt} \propto \frac{\hbar}{X^{elast} + X^{inelas}}$, an expression can be found for the scattering times. This will help evaluate the results , as the broadening of the current density peaks will depend on these scattering times due to this affecting the tunnelling. This is derived using that the diagonal parts of the scattering matrix corresponds to the broadening $\Gamma_{\alpha\beta} = 2\pi X_{\alpha\alpha,\beta\beta}$ [17]. Knowing that only X^{imp} has changed it can be concluded that any changes in τ_{scatt} is due to the increase or decrease in doping density.That is , if the scattering times decrease and the broadening increases it can be concluded that the increase in broadening comes from a dephased tunnelling.

The scattering affects the broadening of the states and the broadening of the states is related to the population of the states. This affects the tunnelling. When the scattering increases , and as a result the scattering time decreases, the states are broadened and the population of states increases. As tunnelling is an elastic process, it can only occur if there is an empty energy slot for the electron. The tunnelling is in tune when the number of electrons tunnelling along the gradient of the field is larger than those tunnelling back. When the population of states increases, the probability of a flow back increases and this dephases the tunnelling current. So when the states are broadened, the "area" where tunnelling occurs increases but the maximum gets reduced.

3.4 Current Density

The programme calculates the current density by evaluating

$$\frac{\psi \nabla \psi}{m}.$$

For further information about how this is implemented the interested reader is recommended to read references [2, 12, 13]. The calculated current density will be plotted against the bias and in this *I-V* curve a local peak will be visible. This occurs when the bias per period is sufficient for effective tunnelling and scattering; this event will often be referred to as a resonance. The current decreases afterwards which is due to a change in resistance where increasing the voltage leads to this decrease in current. This is called *negative differential resistance* (NDR). The NDR hence occurs when

$$\frac{\Delta V}{\Delta I} < 0\,. \tag{9}$$

It is important to note that there are often pre-peaks in the calculated *I-V* characteristics. Often the first peak is when the LLS and the injector state are in resonance, provided the bias at this point is the same as or larger than the longitudinal optical phonon energy. Sometimes there are several pre-peaks. If the bias for the pre-peak is lower than the longitudinal optical phonon energy, then this is probably a peak for a resonance spanning over several periods. This is because the gradient of the system is not enough to get the LLS and the injector state in resonance.

In the scope of this investigation the MF and scattering matrices will change and never be the same for two cases. Instead of investigating the same bias point, which would be the proper choice if the MFs were the same, the resonance peaks (which might occur at different biases) will be investigated more thoroughly. Basing the investigation on

$$J_{max} = \frac{n_{2D} e}{\tau_{trans}} \tag{10}$$

as it is stated in reference [6] on p.137, the local current maximum should increase linearly with sheet doping density, provided that the transport time τ_{trans} remains the same.

3.5 Gain

Gain is achieved when the number of photons escaping the lattice is larger than the number absorbed by it. The gain is defined $g(\omega) = -\alpha(\omega)$. [6] The programme calculates the gain from the real part of the dynamical conductivity $\sigma(\omega)$ (the gain is defined in [2]) i.e.

$$g(\omega) = -\frac{\Re\sigma(\omega)}{c\varepsilon_0\sqrt{\varepsilon_r}} \tag{11}$$

where ε_0 is the permittivity of free space and ε_r is the relative permittivity. The gain thus depends on the inversion Δn and the broadening Γ^{-1} . [6]

There will be losses due to the waveguide material which encapsulates the QCL, re-absorption and mirror losses. The model takes some of these losses into account, the absorption between the states and the empty waveguide. The model does not take free carrier absorption or mirror losses into account. In reference [11] it was reported that the absorption increases with increased doping.

4 The Computation

The types of structures which the QCL constitutes are hard to simulate but there are many different models which can be implemented. In reference [20] different simulation methods are presented. The computer programme uses Non Equilibrium Green's Function Theory (NEGFT) defined in second quantisation in order to calculate the current density and the gain. The model is written by A. Wacker and his colleagues. It allows for a perturbation treatment of the scattering events and the evolution of states. [2] The interested reader is recommended to see references [21], [22] and [23] in which the concepts of second quantisation and Green's functions as their implementations are explained. The current density (qualitatively) and gain (quantitatively) provide a measure of how well the QCL works theoretically.

The first step of the model is to construct the Wannier functions and establish the Hamiltonian for the heterostructure. This is achieved in the programme package called WannierV7.f90. The input file constructed in this step is given the periodicity parameters of the QCL: the layer structure, the energy offsets and the effective masses of the materials (GaAs and $Al_xGa_{1-x}As$). Also the doping region, the doping density $n_{3D} = N_{2D}^i \cdot L_i^{-1}$ (L_i is the thickness of the doping layer), and the number of δ-functions defined. By increasing the number of δ-functions the resolution increases. The WannierV7.f90 programme package calculates and creates files which are then used by the negft7V.f90 programme package.

The next step is to use the negft7V.f90 programme. It calculates the current density and the gain. In the negft7 input file, the number of neighbouring periods and the number of bands are set. The number of energy points and k-space points are set here and this affects the resolution of the calculation. The energy and k-space points should be of the same order of magnitude. The temperature is also set. This temperature will not be the lattice temperature but the temperature of the "heatsink". This means that the lattice temperature will be higher than the "heatsink" temperature for the simulation. The bias interval and the step-size of the bias are also set in this input file. If one wants the same resolution the step-size and the bias interval has to remain constant. (The step-size usually ranges between 0.1meV to 1meV in this investigation.) The gauge is chosen and the number of harmonic indices can be set as well in this input file.

The iteration process is as follows. An initial value of the self-energy is set and this start value varies and is determined by the programme. This is used when the programme continues with calculating the retarded and advanced Green's functions by solving the Dyson equation, see reference [2]. The lesser and greater Green's

functions are calculated from the Keldysh relation. New self-energies are calculated by using the Green's functions. If these new self-energies are not consistent within a tolerance of $5 \cdot 10^{-4}$ to the previous ones, the process starts again by choosing a new start value of the self energy Σ by the Broyden algorithm. This is repeated until self-consistency is achieved. Then the final Green's functions and self-energies are used to calculate the current density and gain. The interested reader can see a full description of this in [2].

5 Laser Samples

The lasers used for this thesis are the QCL samples presented in references [9], [24] and [10]. These structures will from now on be called ***the two well laser***, ***the asymmetric three well laser*** and ***the symmetric three well laser*** respectively. In tables 1, 2 and 3 in appendix A, the constant parameters to the input files can be found.

The two well laser is the simplest structure used during this thesis work. It is (as the name suggests) a two well, two barrier laser, utilising an optical phonon in order to deplete the lower laser state. The layer structure is **3.8**/17.9/**4.5**/8.3 nm giving a period length of 34.5 nm. Bold font stands for barriers, the other font symbolises wells. This notation will be used in the rest of this thesis. The laser is a three state design, where the extraction and injector states are the same state (see figure 4(a)). The transition will be diagonal (see figure 4(a)) as the ULS and the LLS are in different wells. The photon energy should be around 16 meV [9, 13]. The conduction band offset and the periodicity of the laser can be seen in figure 4(a), with the Wannier-Stark states plotted for the first five bands. This laser has been chosen because of its simple structure and will provide a good starting point for the interpretation of the results. There are experimental results for this laser to compare with, see reference [9]; the density study has not yet been performed experimentally for this sample. In references [25] , [11] and [26] they have performed similar studies both theoretically and experimentally on different laser samples. All of them report a linear increase of the threshold current density.

The asymmetric three well laser has three wells and three barriers, see figure 4(b). The layer structure is **4.8**/8.5/**2.8**/8.5/**4.2**/16.4 nm giving a period length of 45.2 nm. The depletion is achieved by resonant tunnelling from the well where the LLS is situated, into the extraction state which is in the next well. It is a diagonal design. The extraction state is in turn depleted by emitting a longitudinal optical phonon, the electron is then injected into the ULS and the process repeats. This laser was chosen because of the similarities with the symmetric three well laser [10], which was one of the main topics in this thesis.

The symmetric three well laser constitutes a diagonal design as the ULS and LLS are in consecutive wells. It can be seen in figure 4(c). The layer structure is **4.5**/8.5/**2.8**/8.5/**4.5**/16.4 nm, the period length will be 45.2 nm. The lower laser state is depleted by tunnelling and then the extraction state utilises an optical

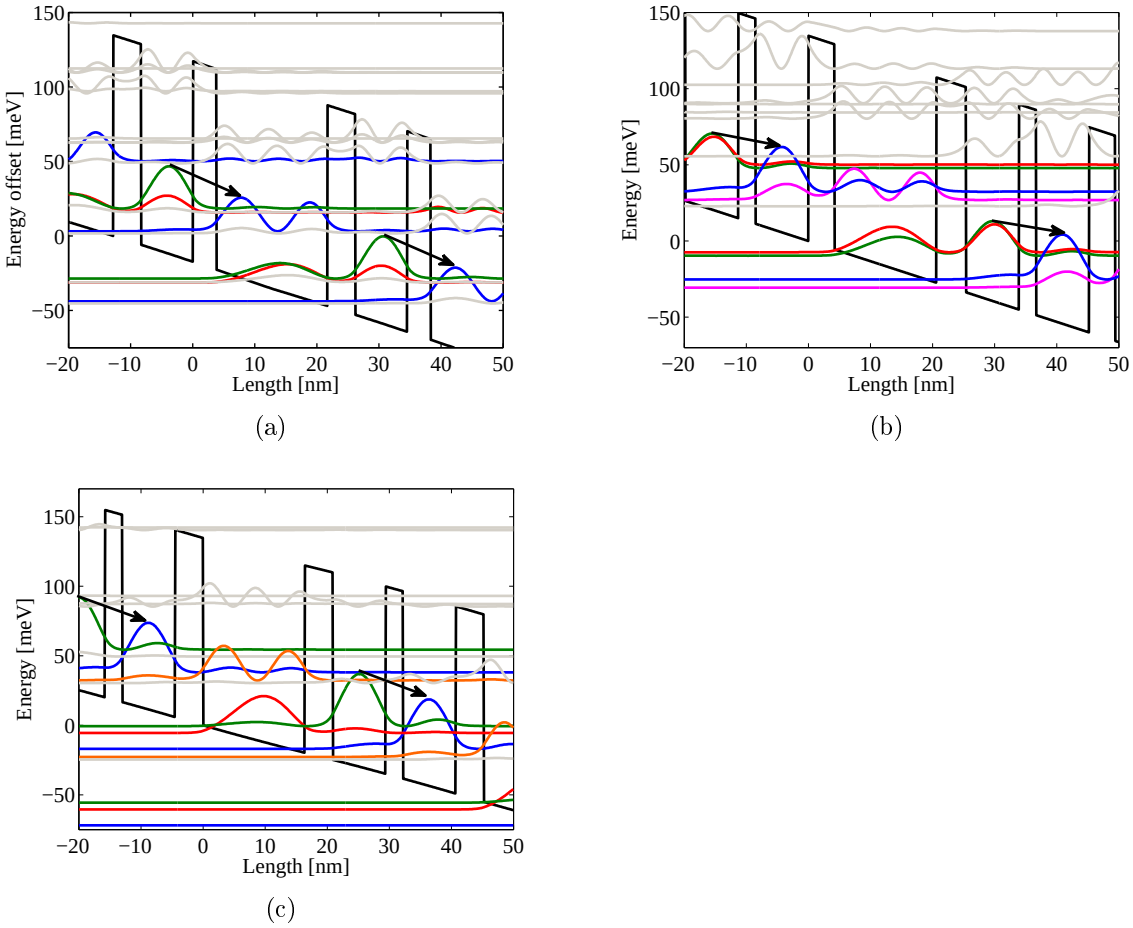

Figure 4: (a)Wannier-Stark states of the two well laser in [9] at a bias of 47mV/period. The ULS is green, the LLS is blue, and the injector/extraction state is plotted in red. The higher states which can provide an escape route for the current are plotted in grey. The doping layer was placed between 11.75nm and 13.75nm for this case (the large well). (b) The Wannier-Stark states at a bias of 57.5mV per period of the asymmetric three well laser [24]. The ULS is plotted in green, LLS in blue, extraction state in magenta and the injector state in red. The doping layer was for this case 1.1 to 3.1 nm. (c) The Wannier-Stark states of the symmetric three well laser [10] at a bias of 55mV per period. ULS is plotted in green, LLS in blue, extraction in orange and injector state in red. The doping layer was for this case placed between 0 and 16.4 nm.

phonon, putting the electron in the injector state to the next period. This structure has been used to investigate dopant migration effects. The structure was then both doped nominally symmetrically and asymmetrically, see figures 17(a)-(b). The structure was chosen as it was used in [10] and the calculated results will be compared with the results of reference.

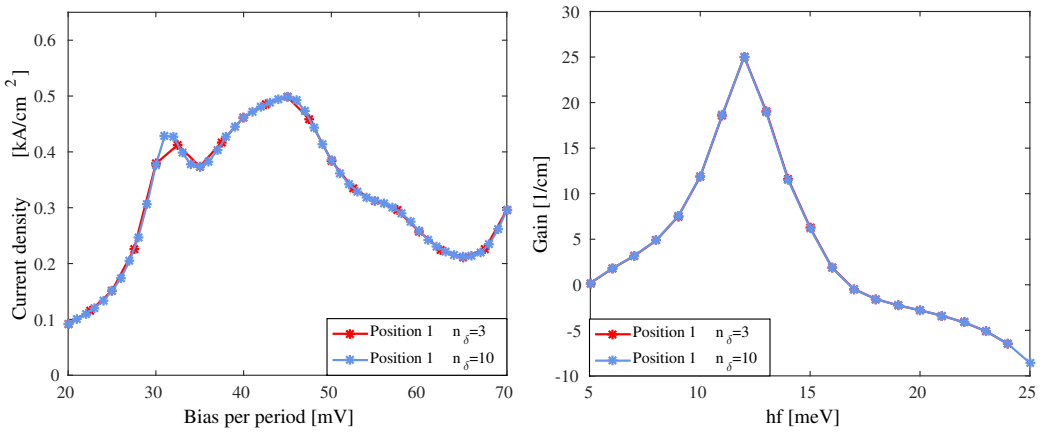

(a) (b)

Figure 5: (a) Calculated I-V curve at position 1 (see figure 11(a)) of the two well laser with three and ten δ - functions. (b) Calculated gain at position 1 of the two well laser, seeing the effect of increasing the number of δ - functions. Five bands were used and the simulation used a temperature of 200 K.

Part II
Results and Analysis

6 The Impact of the Number of δ-Dopings

The calculated I-V and gain characteristics are essentially the same when using three and ten δ - like functions in the simulation, see figure 5 (a) - (b). This suggests that it will suffice to use three δ - functions in the calculations. For wider doping layers the use of three δ - functions have been the rule of thumb. For very narrow doping layers, as for some of the layers in the migrating cases (see section 9), one δ-function was assigned. The number of δ - functions used in each case study can be found in tables (1) - (3) in appendix A.

7 Different Doping Densities

7.1 Implementation

In this part of the thesis the impact of decreasing and increasing the doping density (while keeping the other changeable parameters constant) have been investigated. The values of these parameters can be found in table 1 in appendix A. The MF and the elastic scattering matrix element will change from case to case which makes the results very hard to interpret. Investigating the elastic scattering matrix X^{elast} will provide an entry point for a proper interpretation of the results.

7.2 The Two Well Laser

7.2.1 Current Densities

In figure 6 (a)-(f) the calculated current densities as a function of the applied bias per period are presented. They are placed from smallest to the highest doping density to provide a good overview of the results. The densities are given in the figure entries in units of the original doping density $n_{2D,ref} = 1.5 \cdot 10^{10}$ cm^{-2}.
In figure 6 (a) it can be seen that the current density is very low, giving a maximum current density around 40 A cm^{-2}. This can be predicted by that the number of electrons are only one tenth of the reference. A small shift (in the order of magnitude of tenths of mV) towards lower biases of the lasing resonance can be seen. In figure 6 (b) the same behaviour is depicted, with a maximum current density around 200 A cm^{-2}. Notice that this is five times the previous value, and this is explained by that there are five times the amount of charge carriers. The original doping density, figure 6 (c), has a maximum current density around 370 A cm^{-2} at 47 mV. This is almost the twice amount of the previous value.

The maximum current density continues to increase with increasing doping density and a small shift towards higher resonance bias can be seen in figures 6 (a)-(f). It can also be noticed and that the NDR after the resonance becomes less pronounced with increasing doping. That is the decrease in current density after the resonances becomes smaller - this implies that it is easier for the charge carriers to pass through the period at these biases. Thus the states are more broadened providing a wider channel for the current to pass through. This can be seen in the broadening of the peaks as this increases with increasing density.

It is very hard to say where the maxima lie for the higher doping densities due to the broadening of the peak, so a local maximum has been fitted in order to calculate the gain for the cases. Why the behaviour is so different might be explained by the fact that the MF $\phi(z)^{MF}$ and $X^{imp}_{\alpha\alpha',\beta\beta'}$ change drastically with doping density (especially the latter). As shown in figure 3 (a) the MF depends on the doping density. This MF is used in the model Hamiltonian which dictates where the energy levels arise and the impurity scattering is used in the calculation of the self-energies and Green's functions. The MF will shift the energy levels and X will change the density of states. When more scatterings occur, the scattering times should decrease, which is seen when plotting these as a function of the doping density, see figure 23 in appendix B.

The linear relationship predicted by equation (10) is not observed for higher doping densities, see figure 7 (a). Hence the transport times change considerably with doping density; they increase with increasing doping density, see figure 7 (b). This could be interpreted as the internal resistance of the device increases with doping density, an effect which can be interpreted as the change in the NDR of the I-V plots. In contrast the scattering time decreases with density, i.e the scattering occurs faster, see figure 23 in appendix B. Then this increase in transport times probably comes from de-phasing of the tunnelling coherence, which can be seen in the I-V plot and

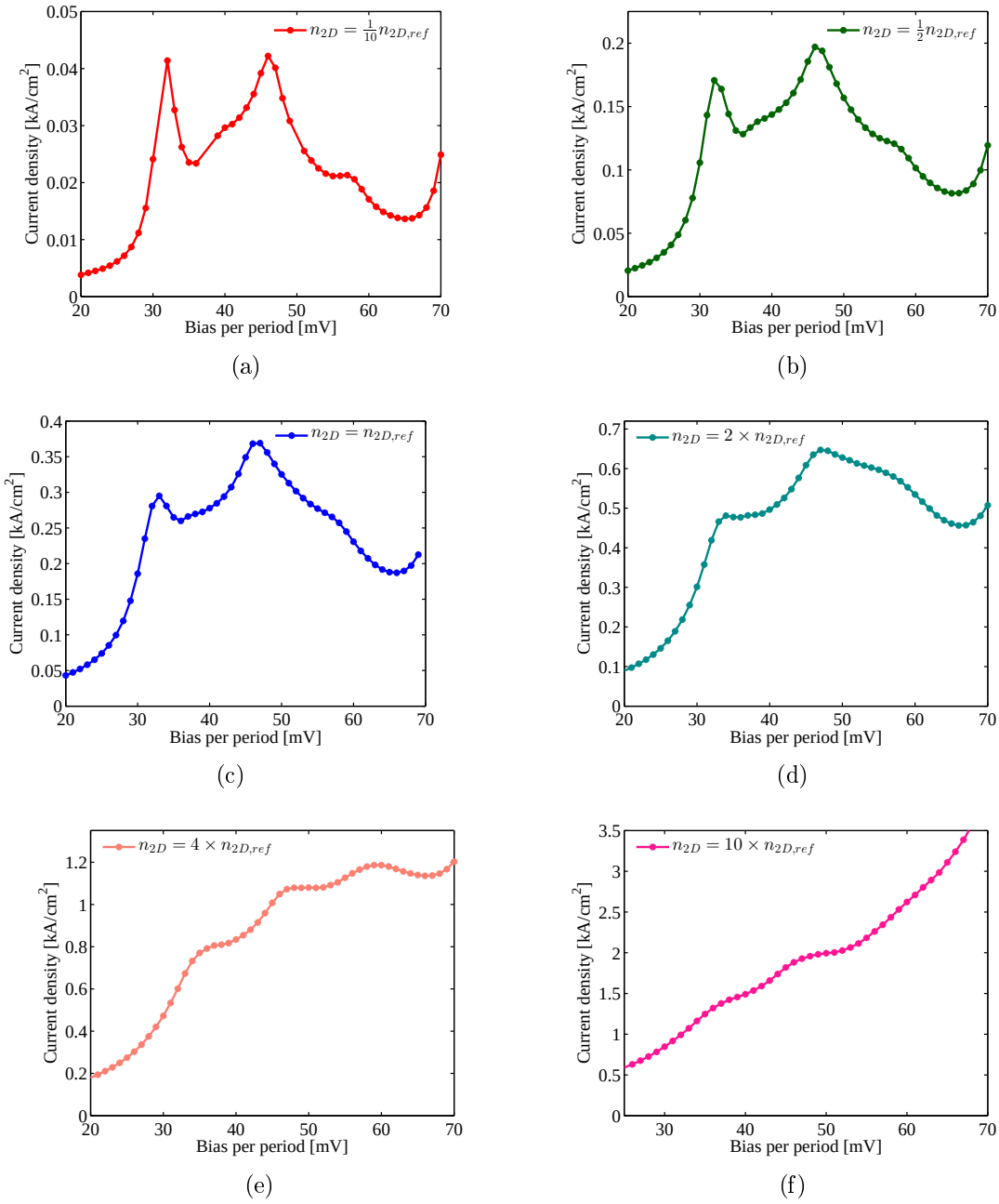

Figure 6: Calculated current densities of the two well laser as a function of the applied bias per period at different doping densities where $n_{2D,ref} = 1.5 \cdot 10^{10}$ cm^{-2}. The calculation was performed at 150 K using five bands. The doping layer was placed in in the extraction/injector well, corresponding to the placement marked in figure 11 (a), position (2). The doping densities can be found in table 4, appendix A with the estimated bias at which the current density is at its maximum value.

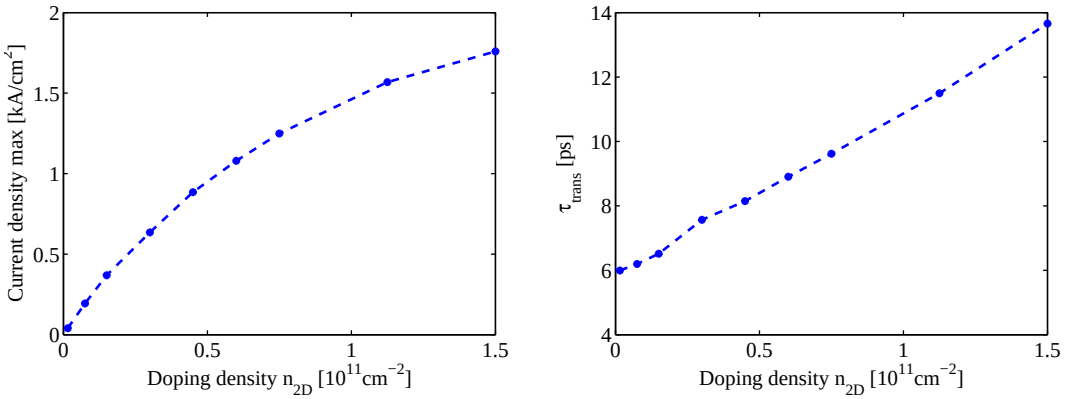

(a) (b)

Figure 7: (a) The calculated J_{max} plotted as a function of the sheet doping density n_{2D}, which was extracted from the programme. The linear relationship cannot be seen here. (b) The τ_{trans} versus sheet doping density n_{2D} calculated using equation (10).

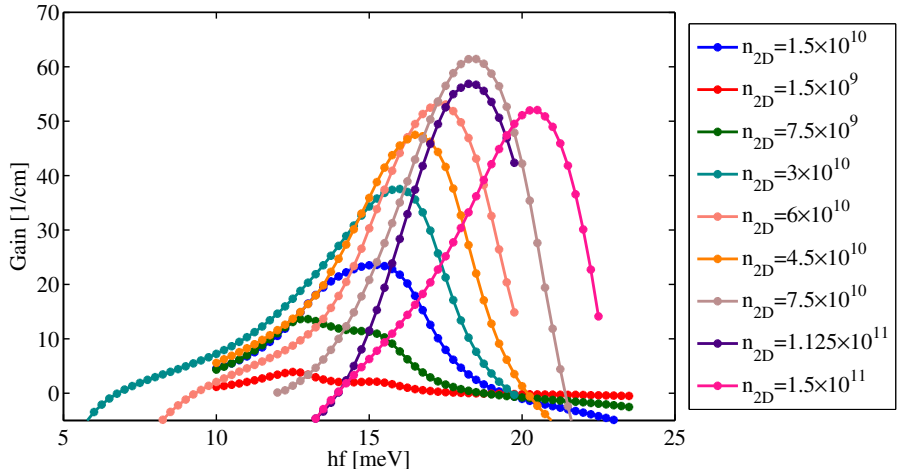

Figure 8: The calculated gain at different densities, at respective laser resonance. The gain has been calculated at 150 K using five bands. The bias per period used for the calculations can be found in table 4 appendix A.

not from the other types of scatterings taking places. This means that when the energy levels become broadened the scattering does not assist the tunnelling and the tunnelling takes longer which was predicted by theory. This effect can be seen in the peak of the current densities. When the peak is thin, see figure 6 (a), the tunnelling is efficient and the tunnelling time is shorter. With increasing density the tunnelling resonance takes longer and becomes a bottleneck for the current, while the scattering time decreases.

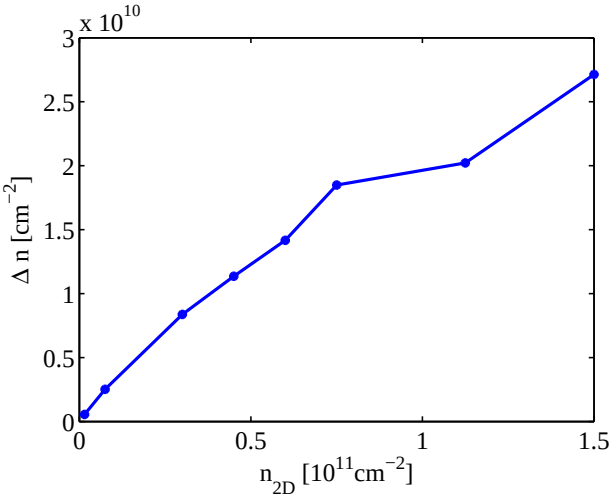

Figure 9: The inversion plotted as a function of the doping density n_{2D} cm^{-2}.

7.2.2 Gain

In the calculated gain, see figure 8, it can be seen that the gain increases with increasing doping density. It can also be seen that the photon energy is shifted towards higher energies. The gain increases as it is a function of the inversion, and when plotting this it can be seen that the LLS is depleted see figure 9 because the inversion increases. This explains why the gain increases with increasing doping. The changing gradient of figure 9 suggests that there are different mechanisms dominant for the different doping densities. For higher doping densities the impurity scattering becomes dominant.

When increasing the number of charge carriers the electric field changes (hence the MF), which shifts the energy levels. This explains the change in the energy of the photon at respective density. For the lower densities both the injector and ULSs are more equally occupied and have a higher overlap of the wave-functions, which explains the two peak behaviour, because the probability is almost equally high for the transition. The transition from the injector to the LLS is then more probable at lower doping densities due to this overlap. At higher densities the transition becomes more "pure", even though a larger number of the charge carriers takes the route through the injector, extraction states. From the calculated gain it is suggested that when increasing the doping density by ten, even though the absence of NDR suggests a stable operating point for the laser the highest doping density does not provide the highest possible gain even though the inversion has increased. So even though the inversion is at its highest the gain is not.

The electron-electron scattering which has been neglected in the model, is of importance here, as this should affect the scattering rate by increasing it, as when the number of electrons increases the number of scatterings increase. I.e electron-electron scattering would destroy the coherence of the tunnelling resonance even more than

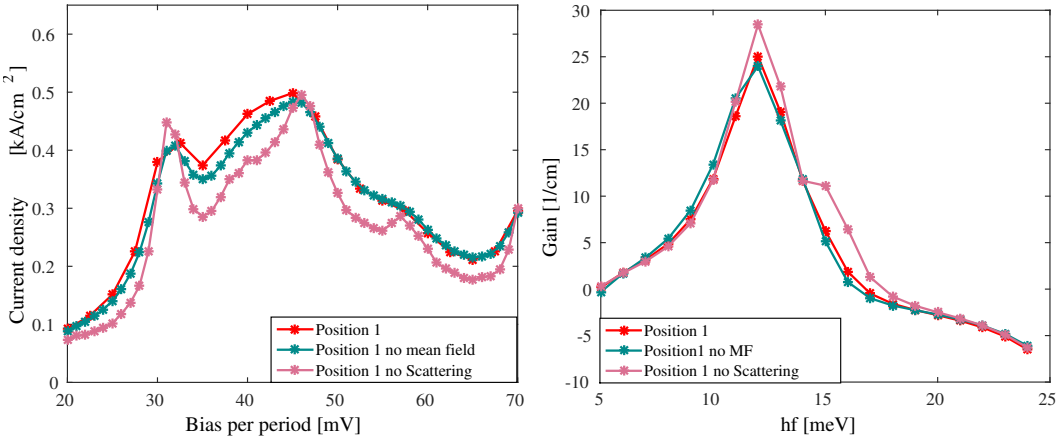

(a) (b)

Figure 10: (a) Calculated I-V curves at position (1) (see figure 11 (a)) of the two well laser with and without MF and Scattering respectively. (b) Calculated gain at position (1), with and wthout MF and scattering respectively. Five bands were used and a temperature of 200 K.

what is seen here, and the transport times would be larger. This accounts for some of the discrepancies between the modelled I-V plots and experimental results at higher densities. The absorption should increase with increasing doping density, as reported in references [11, 25, 26], and the calculated gain may not be as large as predicted in this investigation. This could be a future development of the model, predicting the total absorption of the structure with the free carriers and mirror losses.

7.3 The MF and Scattering

In the previous part of this section the MF and the impurity scattering changed in each case. That there are two effects at the same time makes the results hard to interpret. Simulating one of the cases without the MF and then without any impurities can help bringing insight into what happens. In figure 10 (a) the calculated current densities for one position can be seen. Here the input file was in one case without any impurities added but with the MF. The other was without the MF present but with scattering.

It can be seen that where the resonance occurs gets shifted to higher biases by 1mV for the case without the scattering, and the resonance is at the same bias without the MF. The I-V plot without the MF looks essentially the same, except that the current density is slightly smaller (at least until the resonance bias, after that point the I-V plots look the same). Without scattering the peaks are less broadened, i.e the tunnelling occurs more effectively as there is no scattering which can inhibit the motion of the charge carriers. Several bumps are also visible in the I-V plot without impurity scattering. This suggests that there are several biases where tunnelling is

effective.

In the gain, see figure 10 (b), it can be seen that the photon energy is similar in all cases. Looking at the Wannier - Stark states, see figure 25 (a) - (c), the energy differences between the ULS and LLS are 11.6 meV for the case without MF, 12.0 meV without scattering and with both the contributions the photon energy is 12.2 meV. Without any impurity scattering the gain increases, and there is evidence of two photon energies, one around 12.2 meV and the other around 15.6 meV. This indicates that without the impurity scattering, the ULS and injector state both induce photon transitions.

8 Impact of Position

The next part of this thesis investigates the impact the position of the doping layer has on the calculated *I-V* and gain characteristics. In theory [6] it is stated that it is beneficial to dope the active region, because this feeds the transition and the inversion. It should also be good to dope the injector region as well in order to provide a more stable electrical field across the structure. [6].

8.1 Implementation

A single doping layer was moved throughout the period of the QCL. Then the current density and the gain were calculated. Here the MF shifts along the z-axis. Also having two slices of doping layers, one in the injector region and one in the active region, has been simulated. The positions of the doping layers can be found in tables 5 and 6 of appendix A for the two well and asymmetric three well cases. The figures depicting this can be found in figures 11 (a) - (b).

8.2 The Two Well Laser

8.2.1 Current Densities

It can be seen in the *I-V* plot, see figure 12(a), that doping different barriers (positions (1) and (3) in figure 11 (a)) produces a similar behaviour of the current density (plotted in red and green). The behaviour of the current densities when doping the wells, positions (2) and (4) in figure 11 (a), is very different see figure 12 (a). Notice that the resonance peak has shifted for the well where lasing is initiated (position (4)) and the well where the electrons are extracted and injected to the next period (position (2)). The broadening of the peaks is qualitatively the same when doping the barriers, but is different when doping the wells.

When the position of the doping layer changes the scattering and MF change in response. The electrons will experience the same periodic structure differently. Also the electronic states will be shifted from case to case which is seen in the *I-V* characteristics as the current density is higher and has another resonance where the injector and ULS aligns (besides for the barriers). Higher current density does not

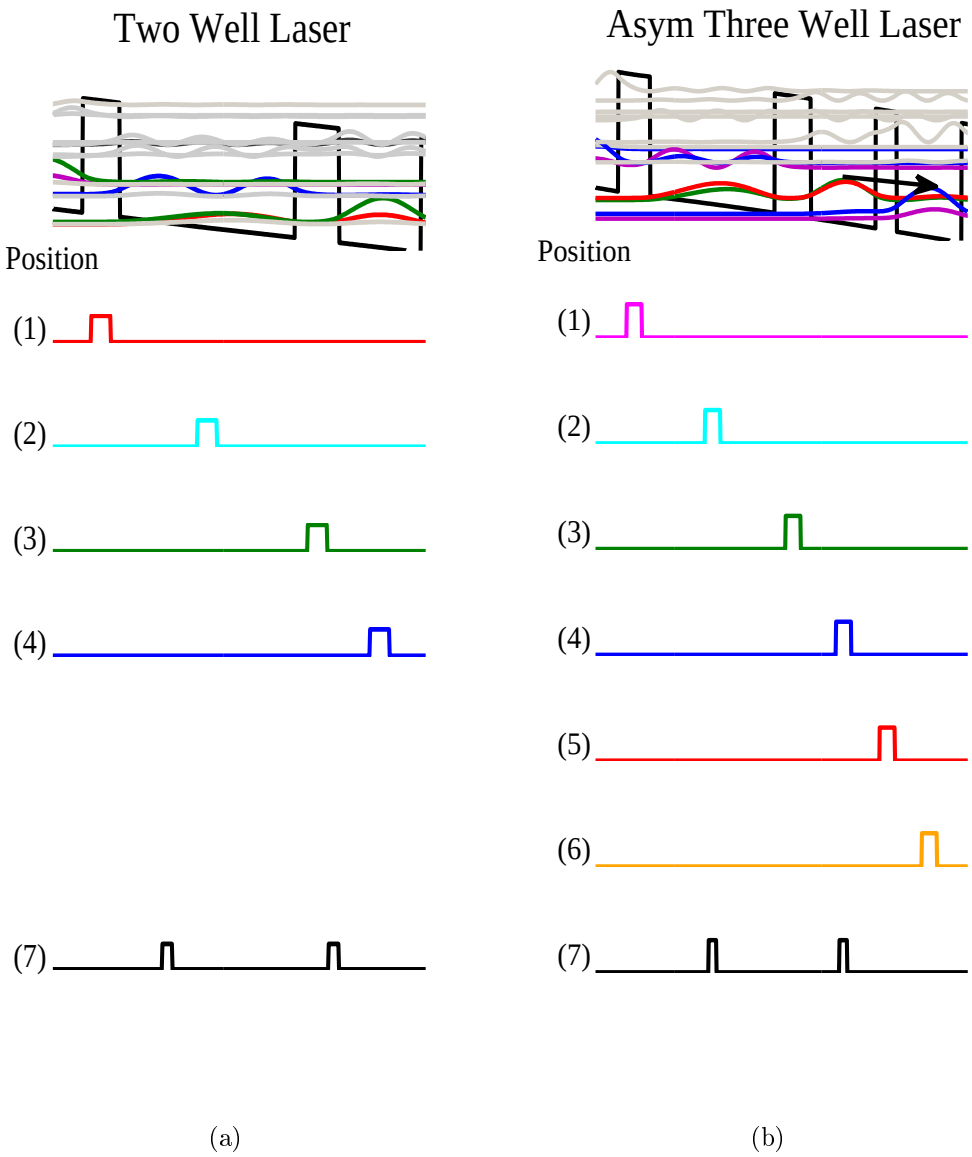

(a) (b)

Figure 11: The Wannier - Stark states of the (a) two well laser and (b) asymmetric three well laser. The different doping layers which have been subject to the investigation are presented below the Wanier-Stark states at the corresponding z-coordinates. (a) Bias 47 mV per period. The doping layers are in red, cyan, green and blue describing each case. These will for further reference be called, position (1), position (2), position (3) and position (4) respectively. The doping layers marked in black depict the case when half of the impurities are in the extraction/injection well and the other fraction in the laser well and will for further reference be called position 7. For details about the doping layers see table 5 in appendix A. (b) Bias 60 mV per period. Position (1) is the reference position used in [24]. For details about the doping layers see table 6 in appendix A. The *I-V* curves and gains will be plotted in the corresponding position colour for each laser sample.

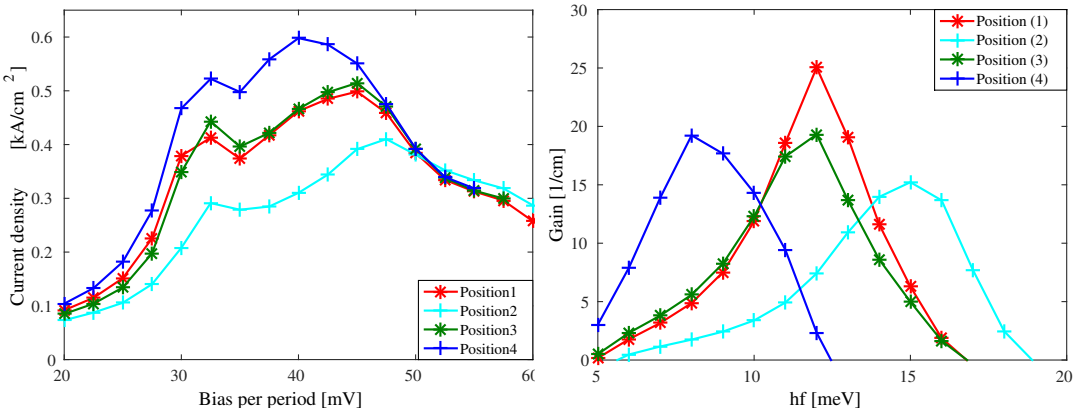

(a) (b)

Figure 12: (a) Calculated current density as a function of the applied bias per period of the two well laser [9]. (b) Calculated gain for the different positions. The gain was calculated at the biases given in table 7 in appendix A. The simulation temperature was 200 K and five bands were used. Each colour represents the colour of the layer given in figure 11 (a) and table 5.

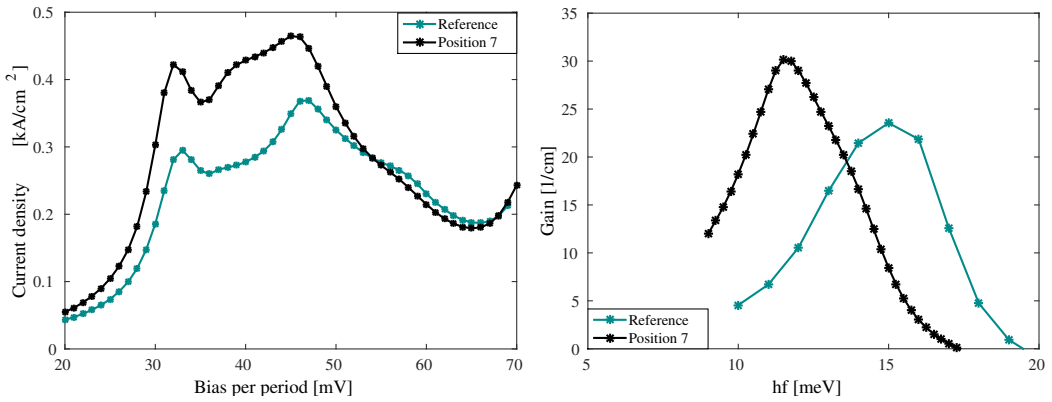

(a) (b)

Figure 13: The original dopant position (position (2)) versus putting half of the impurities in respective well of the two well laser. (a) These current densities were calculated at a temperature of 150 K. (b) The calculated gain. Five bands were used and the simulation used a temperature of 150 K. The gain was calculated at 45.0 mV per period (black) and at 47.3 mV per period (cyan).

necessarily imply higher gain, as the gain depends on the inversion of the states. Will the similarities between the red and green I-V curves (positions (1) and (3)), give the same gain? They should have the same photon energy, as they have the same resonance peak in the I-V plot.

The case when placing half of the impurities in each well (they of course sum up to the same doping density $n_{2D} = \sum_i L_i \cdot n_{3D,i}$) has been simulated as well, but at a temperature of 150 K. [1] In figure 13 (a) it can be seen that the current density increases, but almost gives the same behaviour of the I-V curve as for placing all the impurities in the extraction/injector well. Almost the same resonances are seen, the pre-peak and the lasing peak, however the peak is at 45 mV per period for the black case, and at around 46 mV per period for the cyan case, so a slight shift in the resonance peak can be seen. The black curve has more broadening to its second peak and a more pronounced NDR after the resonance. This indicates that the flow of the current is helped by placing the doping layers in different wells. This is due to a more stable electric field over the structure and the fact that the impurity scattering depletes the ULS.

8.2.2 Gain

A huge difference between the positions can be seen in the gain, especially between the positions (2) and (4) (see figure 12 (b)). Doping the barriers (positions (1) and (3)) gives the same resonance and a photon energy around 12 meV. However they have different gain, so it is better to dope the laser barrier, position (1), than the injector barrier, position (3). In figure 13 (b) it can be seen that the photon energy for the last position study, position (7), is around the same energy as for the first and third positions. The behaviour of the gain at positions (2) and (4) are very different; they have different photon energies (they differ by 9 meV). This difference in photon energy was indicated by the I-V plot. The gain is highest for the case when placing all the impurities in the laser barrier. In figure 13 (b) it can be seen that the gain (at 150 K) is much larger for the case when doping two layers, one in each well of the two well laser, compared to just one well.

8.3 The Asymmetric Three Well Laser

8.3.1 Current Densities

In figure 11 (b) it can be seen that seven cases were simulated where the doping layer had been located around the center of each well and barrier. Also the case of having half of the impurities in one well, and half in the other, has been simulated. This latter case is depicted by the black bars in 11 (b). The current densities are plotted in the same colour as the slices. In figure 14 (a) the different I-V curves for the different positions can be seen. The current densities when placing the doping layer in the different wells are lower than when the doping layer is placed in either

[1] Preliminary results of this thesis work were presented at the international workshop IQ-CLSW2014 (Policoro, Italy), and the results presented there were simulated at 200K.

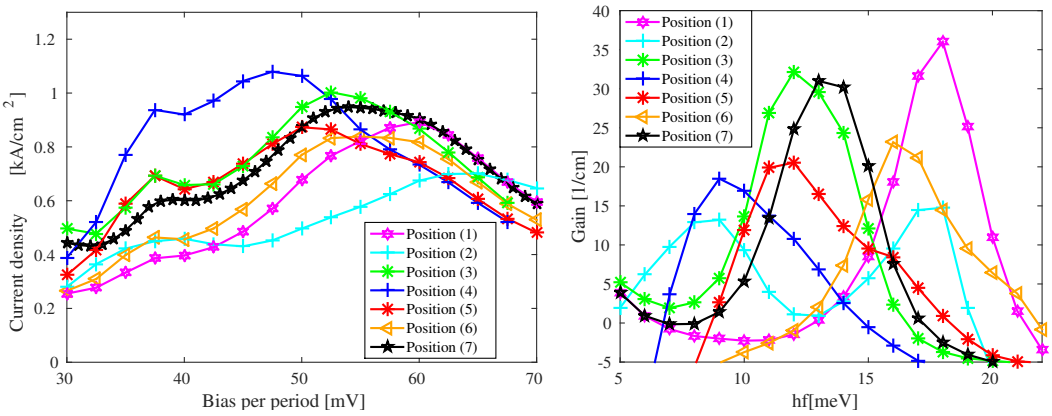

(a) (b)

Figure 14: (a) The calculated current densities. Position 1 is the reference. (b) The calculated gain. The simulations were performed using the laser given in Ref [24]. Eight bands were used and the simulations were run at a temperature of 200K. The gains were calculated at the resonance bias, which can be found in table 8 of appendix A.

of the barriers with the exception for position 4 (see figure 14 (a)).

Hence the photons will have different energies at different positions. As the gain depends on the inversion of states and cannot be predicted by just using the I-V plot. This statement can be argued for by looking at the results from the two well laser [9], when comparing that the case giving the highest current density did not produce the highest gain.

8.3.2 Gain

Here the first position, that is placing the doping layer in the first barrier of the period, gave the highest gain. This is the original design described in reference [24]; the gain plotted in magenta 14(b). It looks like the peak is very "pure", i.e that only the transition from the ULS to the LLS occurs. The photon energy is around 18 meV. The other strong gain is received from placing the doping in the second barrier. Here the photon energy is around 12 meV. The third highest gain comes from placing a doping layer in two of the wells (see black position in figure 11 (b)). The photon energy is around 13 meV. The gain produced from the sixth position, the orange case (the last well in the period), has the fourth highest gain. The photon energy is around 16meV. This peak has a small bump at higher energies which indicates broadening due to another transition from other states which are in resonance at this bias (giving a photon energy of about 20 meV). The gain from placing the doping layer in the third barrier (fifth position), the red case, is the next in line, and it looks the same as for the sixth position, but it is shifted towards lower energies. The photon energy in this case is around 12 meV. The gain when placing the doping layer in the second well gives a photon energy around 9 meV. This suggests that the

gain depends where the doping layer is placed.

Assuming this laser structure will have losses of 20-25 cm^{-1} the laser has to have a higher gain than this in order to efficiently lase. Hence placing the doping layer in the first barriers, or placing the impurities by equal amounts in different wells will produce a laser with high gain. The position also affects the photon energy, which needs to be considered when placing the doping in the structure.

9 Dopant Migration Effects

9.1 Background to the Study

Having a symmetric structure, as the QCL presented in reference [10], the I-V characersitics should look the same independent of the bias polarity. This is because the electrons experience the same potential wells and barriers in either direction. In the model this would translate to that the mean-field and the scattering potentials would be the same, so irrespective of bias polarity the results would be the same as well for the symmetric doping profile. In the previous part of this thesis it was found that the doping profile is very important as different doping profiles provide different laser output. So the different doping profiles used will give different output for the same bias polarity, but will the opposite polarity give the same current output?

In reference [10] a symmetric QCL was investigated experimentally, were one sample had a nominally symmetric doping profile and the other sample a nominally asymmetric one. The symmetrical doping profile should give the same I-V characteristics independent of bias polarity while the asymmetrically doped sample should have a bias dependence. In reference [10], see figures 15 (a) - (c), it was found that both doping profiles give different V-I characteristics at different bias polarity. The optical output should be the same but it can be seen, see figure 16, that there is a bias dependence for both the samples. This is not what was predicted. The hypothesis in ref [10] explaining this outcome is that there is dopant migration. This would give another doping profile than the one which was predicted and would account for the asymmetry. This part of the thesis will investigate if dopant migration actually can account for the bias dependence of the current density and gain characteristics.

9.2 Implementation

First the doping cases without migration were simulated. This was done in order to see if there are any similarities between the results in reference [10] and the non migrating cases. Also this was done in order to serve as a comparison for the model to see if the diffusion effects will be visible. Figure 17 (a) shows the nominal doping profiles, two of them are depicted in [10]. Then diffusion was added to the input files, and these scenarios can be seen in 17 (b) where the orange profile symbolises the case when the diffusion of charge carriers had created a more or less homogeneously thick layer. Profiles (1) - (3) have had very soft migratory effects where the doping profile and thus the sheet densities of the layers were predicted making an ansatz

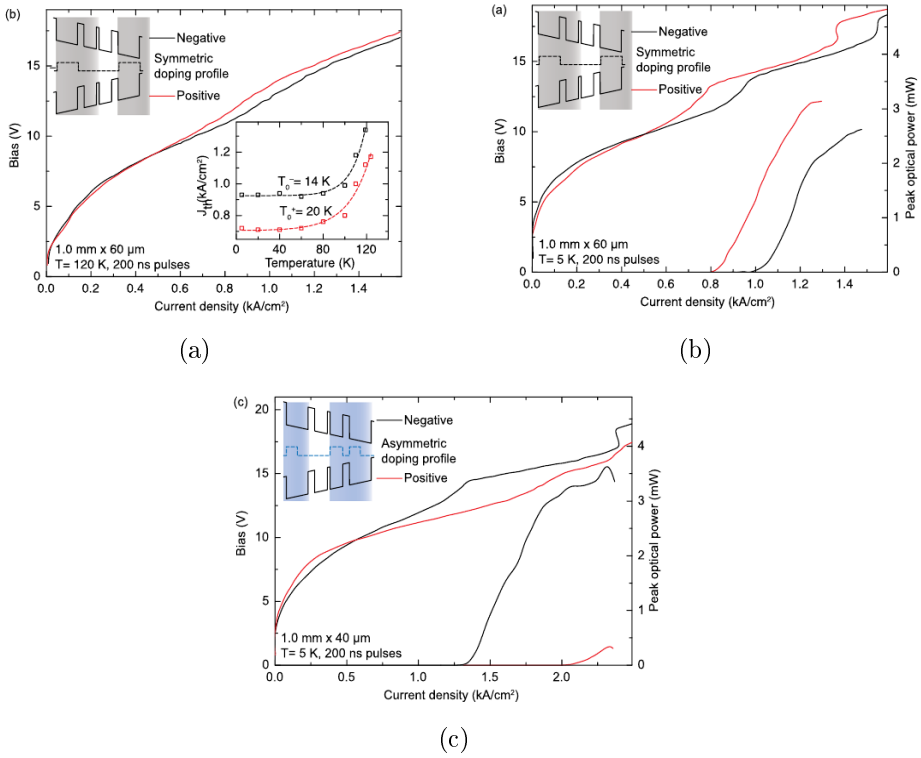

Figure 15: The experimental V-I characteristics are taken from Ref. [10]. The sheet density is $n_{2D,ref} = 3.28 \cdot 10^{10}$ cm^{-2}. The measured current density is plotted as a function of the total bias over the laser at (a) 120K and (b) 5K for doping profile (1)(see figure 17(a)) and in (c) at 5K for doping profile (3), see figure 17(a).

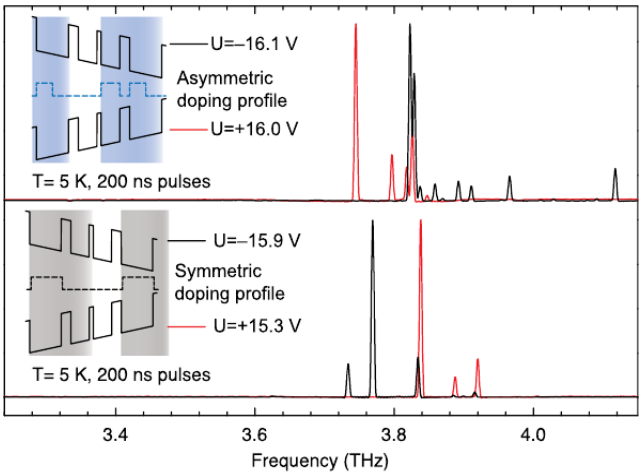

Figure 16: The measured optical output of the QCL used in [10]. The figure is taken from [10].

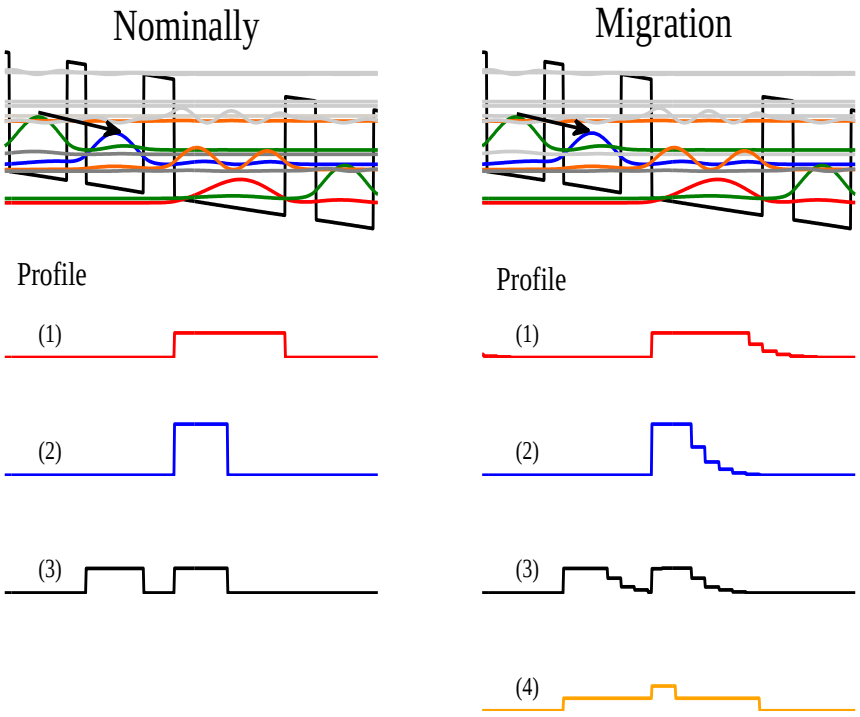

s

(a) (b)

Figure 17: Wannier - Stark states of the symmetric three well laser and the band structure. The positions of the doping layers at the corresponding position in the period is given. (a) The non migrating cases, the nominally doped samples. (b) Diffusion effects have been added. In profile (4) it has been assumed that there is diffusion from one of the doping layers into the other giving an extra effect in the doping profile. Note that there is a whole well and barrer unaffected by the impurities. The total number of impurities is the same. It has been assumed the diffusion is along the growth direction. For further information about the doping layer see tables 10 - 12 in appendix A.

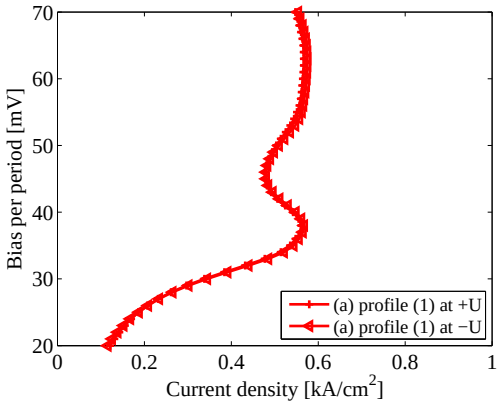

(a) Profile (1)

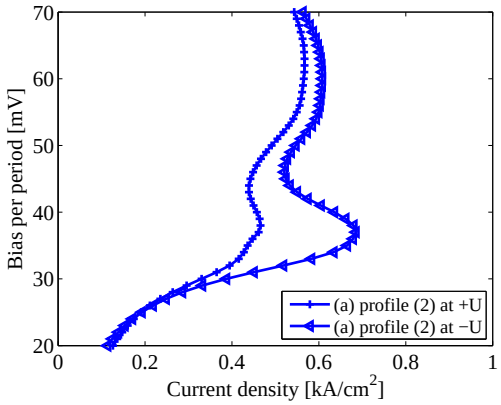

(b) Profile (2)

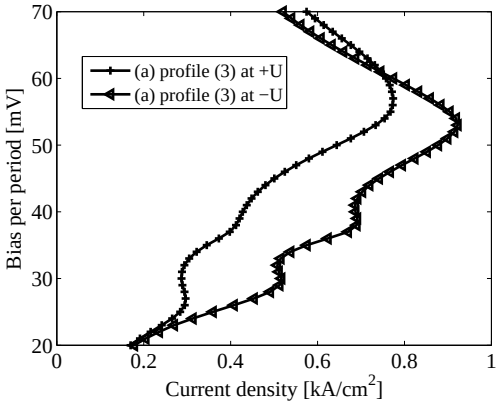

(c) Profile (3)

Figure 18: The calculated V-I plots for the different doping profiles (1) - (3) see figure17 (a). Note that the V-I curves have been plotted in the corresponding profile colour. These current densities have been calculated using five bands and a temperature of 200 K.

to the solution of the diffusion equation of the form $exp(-z/D)$, where D is the Debye length. This can be seen in figure 17 (b), profiles (1) - (3), where the height of the doping is correlated to the sheet density. It is important that the sum of the impurities is the same as in the non migrating case, as it otherwise would be hard to interpret the results i.e

$$n_{2D} = \sum_i L_i \cdot n_{3D,i} \,.$$

9.3 Without Dopant Migration

In order to get a good overview of the results all the V-I plots, with the doping layers presented in figure 17 (a), profiles (1) - (3) will be presented shortly in order to facilitate the rest of this section. What will be seen can be predicted by the previous section where different doping position will give very different V-I curves. Here the polarity dependence will be specified and discussed before the dopant migration is added. Note that the x-axis is the current density and that the y-axis is the bias

per period. This change in plotting the calculated current density has been made in order to simplify the comparison between the reference results and the results of the simulation. The calculated current density at negative polarities has been chosen to be plotted with the reverse sign in order to facilitate a comparison between the two curves. In figure 18 (a) the absolute values of the current densities at positive and negative polarities are plotted. The doping profile is symmetric, accounting for the behaviour of the current density, which is the same. This is due to that the potential the electrons experience is the same and the scattering occurs at the same places independent of polarity. There are some small differences; however, these can probably be accounted to the error due to the approximation simulation uses. These errors depend on that the programme does not look at one period only but at the neighbouring periods as well. This gives rise to the small asymmetry as one of the neighbouring periods will end with a well and one will end with a barrier. It can be noted that these *V-I* characteristics are not very similar to the reference plot, see figure 15 (a). Note that there is actually a pre - peak in the experimental results which should correspond to the pre - peak in the calculated current density at around 37 mV per period.

In figure 18 (b) the calculated current densities for the second doping profile can be seen. This profile has no experimental result to be compared with, but it was simulated both for being part of the position study and migration effects. Profile (1) can be interpreted as the migrated case of profile (2). Here a large difference and a clear polarity dependence can be seen. Also the position where the scattering occurs changes. Essentially, all the impurities have been condensed to a smaller volume in the period, see figure 17 (a) profile (2). Hence the MF will have a higher amplitude and the energy levels will be shifted more in this region (still a small effect). There is a huge difference in the behaviour between 30 mV per period and 55 mV per period, where the negative polarity gives higher current densities. The resonance where the injector level and the extraction level align provides a better channel for the current to be transported through at the negative bias. At positive bias, the tunnelling is not as coherent when the injector and extraction states align. The difference between the *V-I* curves is due to the asymmetry of the doping. The potential of the wells which interacts with the electron will be different (the MF will be the same but it will look different depending on which direction the electron is coming; and also on where the scattering occurs changes). Hence different polarity shifts the states differently.

In figure 18 (c) the calculated current densities for the third doping profile can be seen. Here a huge difference between the current densities at different polarity can be seen, see figure 18 (c). This can be explained by that the doping profile is so different to the first one. When the doping is placed in this manner (see figure 17 (a), profile (3)) the conduction band edge will bend at both the doping positions. The last well should be structurally the same, independent of bias when the electron pass through it, but the states will be shifted to the nominal case. However, how the electrons will experience the potential of the extraction/injector well depends on the polarity of the bias and also where the scattering occurs changes. When

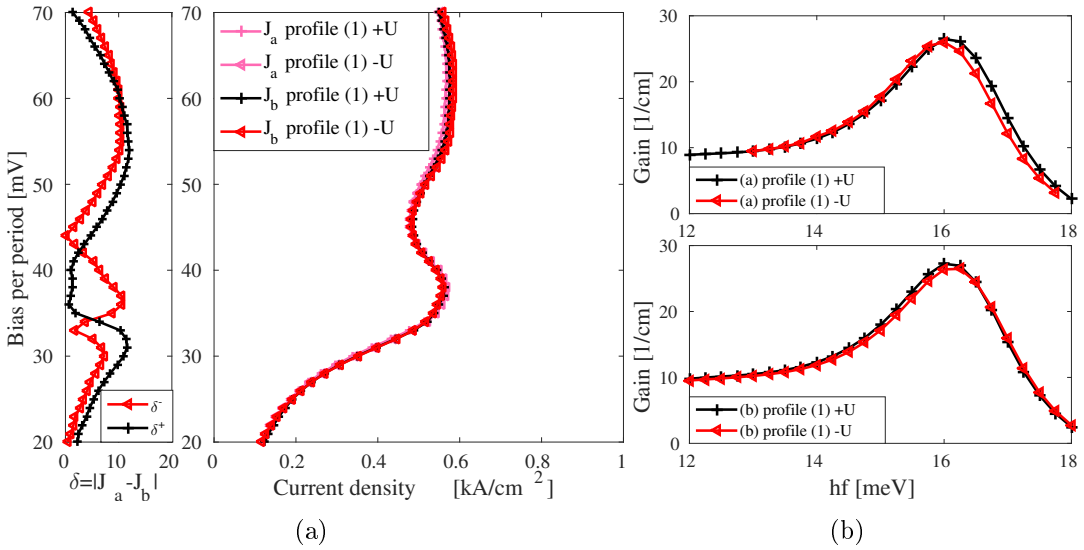

Figure 19: The calculated current densities for the doping densities presented in figure 17 (a) - (b) profile (1). The change $\delta = |J_a - J_b|$ has the unit of $\mathrm{A} \cdot \mathrm{cm}^{-2}$. (b) The calculated gain without (a) and with (b) doping migration. The nominally doped case is in the upper plot using different symbols and colours naming the polarity. The migrating case have been plotted in the lower plot. Five bands were used in the calculation and the temperature was 200 K. The gain was calculated at the biases given in table 14 of appendix A.

comparing this *V-I* plot to its reference, (see figure 15 (c)), the two are similar but not completely the same. They are similar in the manner that this profile give a higher current density (but not as high as the reference). The separation between the resonance bias where lasing occurs is differentiable like in the reference. However there are discrepancies between them, as more resonances at higher biases can be seen in figure 15 (c), the gradients are not the same and there is one more pre-peak in the calculated *V-I* plot. It can be noted that experimentally they received more than twice the current for profiles (1) and (3). This discrepancy might be due to the fact that the doping density in reference [10] is only estimated and might be higher. Still it has to be remembered that the model lacks electron-electron scattering.

9.4 Doping Profile (1)

We now concentrate on the red doping profiles, the cases with and without dopant migration as shown in profile (1) in figure 17(a) and (b). The case without dopant migration is shown in subfigure (a) J_a will be the calculated current density without dopant migration and J_b with.

9.4.1 Current Densities

The *V-I* plots in figure 19 (a) have been calculated without (pink) and with (red and black) migration effects. In figure 19 (a) it can be seen that there is a slight

difference between the polarities. Both the *V-I* characteristics have the same pre-peak which is not seen experimentally at these higher temperatures (see figure 15 (a)) but it is more pronounced experimentally at lower temperatures (see figure 15 (b)). When adding migration effects, (see figure 19 (a)) there is a slight increase in the calculated current density after 45 mV per period. The discrepancies between the polarities can still be credited to the programme, as the $\delta = |J_a - J_b|$ is very small. Thus there is no difference between the nominal and migrating case indicating that the diffusion effect had been underestimated.

9.4.2 Gain

The gain characteristics have also been calculated in order to see if any considerable effects occur which are not predicted by the *V-I* plot. In figure 19 (b) it can be seen that there is a slight blue-shift of the peak at the positive bias, giving a photon energy of 16.25 meV, the negative bias giving a photon energy of 16.0 meV. In figure 19 (b) the gain with migration effects has been plotted on its own under the unmigrated case. Here it can be seen that the gain increases slightly and that the peaks change photon energy. Now the gain at positive bias (plotted in black) peaks at 16.00 meV and the calculated gain at negative bias peaks at 16.25 meV. Hence, based on these curves there is a slight shift to the red at the positive bias and a shift to the blue at negative bias. Fitting a Lorentzian to the negative bias cases give that the peak is at 15.96 meV with no migration and 16.03 meV for migration (so a slight blue-shift at the negative bias). The difference is smaller with the fit. Even-though there is a small shift visible the results do not suffice in order to conclude that this is due to dopant migration or due to the simulation. This shift in peak energy from the nominal case to the migrated case might be due to the resolution of the simulation. It could also be that migration effects have been underestimated, which would not affect the mean-field or the scattering that much, which in turn affects the calculated results.

Without migration effects the picture should look the same at the start or the end of the doped region (independent of which direction the electron travels). However at the end of the doped region in the migration case there will be fewer charges relative to the non migration case, so the doping region has extended beyond the barrier into the next well.

9.5 Doping Profile (2)

9.5.1 Current Densities

In figure 17 (a) - (b), profile (2), the structures had been asymmetrically doped both nominally and with migration effects; the calculated current densities and gain can be seen in figure 20 (a)-(b). When adding migration effects, see figure 20 (a), the pre-peak decreases slightly at the negative bias, but the pre-peak increases slightly at the positive bias. It can be seen that the difference $\delta = |J_a - J_b|$ is very small. The *V-I* characteristics look essentially the same.

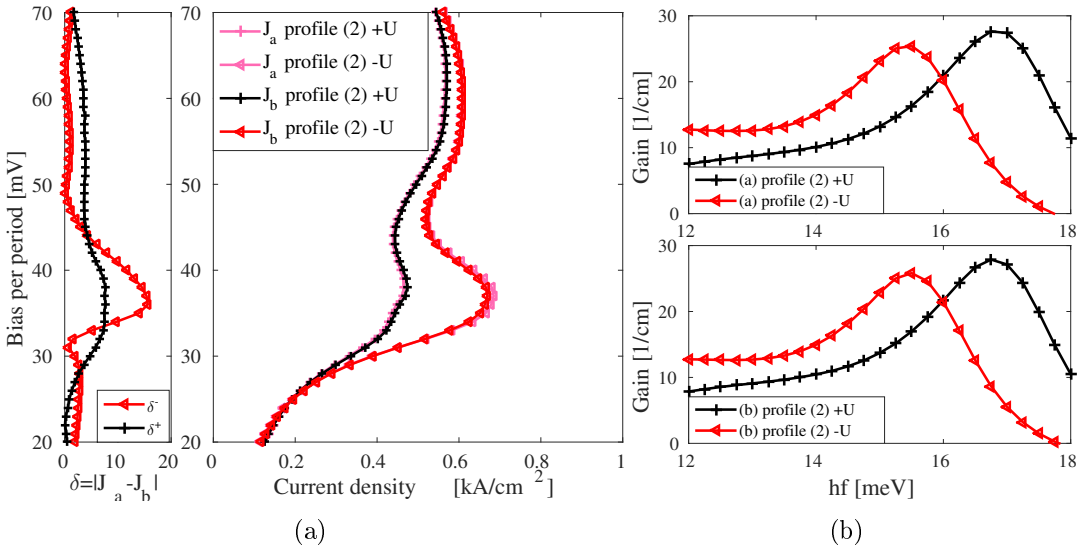

Figure 20: (a) Calculated current densities for the asymmetric doping profile given in 17 (a) - (b) profile (2) and the difference δ ($\mathrm{A} \cdot \mathrm{cm}^{-2}$) between the unmigrated and the migrated case. (b) The calculated gain. The nominally doped case is plotted in the upper plot using different markers and colours for the polarity. The migrating case has been plotted in the lower plot. Five bands were used and the simulations run at a temperature of 200 K. The bias used for the calculation of the gain can be found in table 14 of appendix A.

9.5.2 Gain

In figure 20 (b) it can be seen, that even though the *V-I* characteristics look somewhat the same at these biases (i.e the same resonance bias), the photon energy is not the same and is separated by 1.25 meV between the two polarities. The calculated gain at negative bias gives a photon energy of 15.5 meV. At positive bias the photon energy is 16.75 meV. The photon energies can be predicted from the Wannier - Stark states, see figure 24 (a) - (b). The photon energy is then predicted to be 16.0 meV at negative bias and 16.6 meV at positive bias. This is not what is given by the calculated gain. This shift could arise from the broadening of the states or that there is some interaction present which lowers the energy of the ULS at negative bias and lifts it at positive bias. Dopant migration effects have also been added and the photon energies will be the same. More over it can be seen that the gain has increased slightly. These differences between the non migrating and migrating case are probably due to the approximation of the simulation.

9.6 Doping Profile (3)

This doping profile will have experimental results to be compared with.

9.6.1 Current Densities

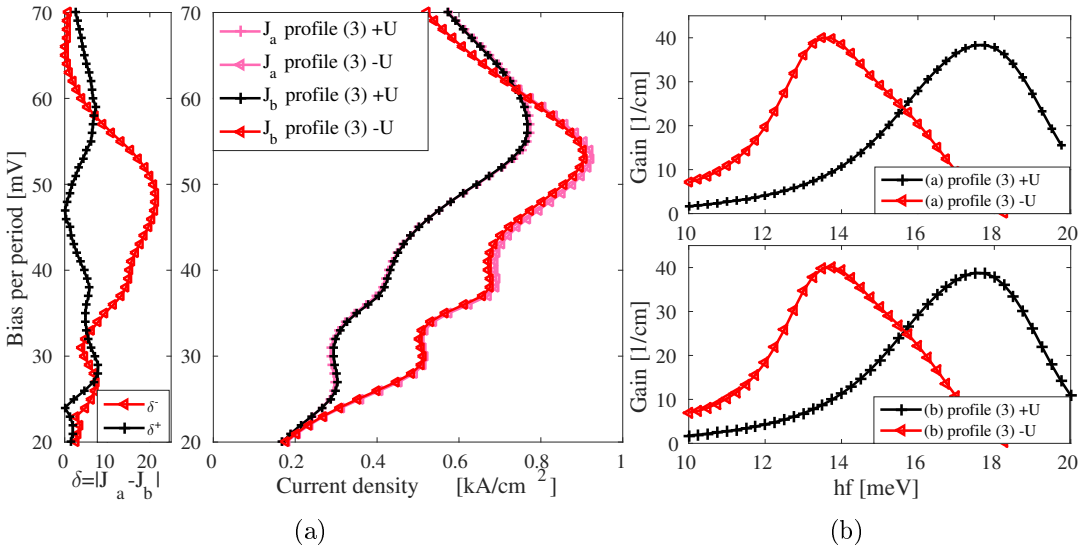

Figure 21: (a) Calculated current densities of the symmetric three well laser figure 17 (a) - (b) profile (3) and the difference δ (A$\cdot$cm^{-2}) between the current densities The nominally doped case has been plotted in pink and the migrating case in red and black. (b) The calculated gain. The upper plot is the unmigrated case and the lower plot with migration effects. The biases which the gain was calculated at can be found in table 14 of appendix A. Five bands and a temperature of 200 K have been used for the simulations.

There is no considerable change in the *V-I* plots when migration effects have been added. The difference $\delta = |J_a - J_b|$ A cm^{-2} is very small. In the *V-I* plot we see three peaks, two pre-peaks and the resonance. The resonance has a bias dependent maximum occurring at -53 mV and at +57 mV, just as for the unmigrated case.

9.6.2 Gain

Calculating the gain at -54 mV and even -55 mV gave very broadened peaks, indicating two photons. A laser transition from the injector state to the LLS thus accounts for the second photon energy. Hence the same bias is used ($\pm$)57 mV for the gain. The *V-I* characteristics indicate NDR which is not a stable operating point (experimentally) but the gain is larger there.

Comparing the calculated gains in figures 19 - 20 (b), the gain is much higher for doping profile (3) than both the previous ones! This was indicated by the position study using several slices, as this would feed the transition with charge carriers and effectively deplete the LLS. In order to have an operating laser the gain has to be larger than the losses which are usually around 20/cm. As for the previous profile the gain is essentially the same for non migrating and migrating cases.

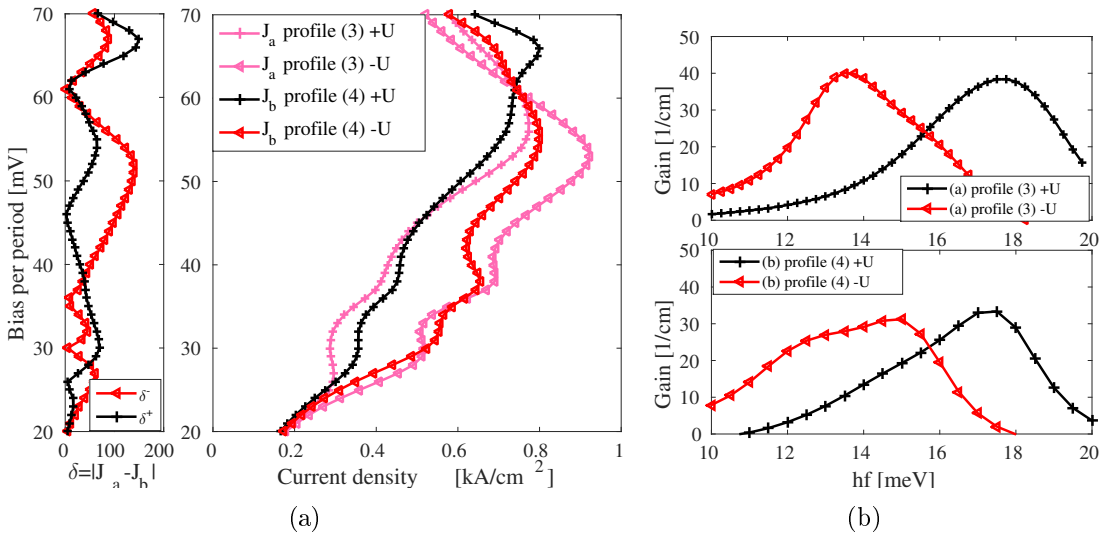

Figure 22: (a) Calculated current densities for the doping profiles see 17 (a) profile (3), and (b) profile (4). (b) The calculated gain. Five bands were used and the simulation temperature was 200 K. The nominally doped case has been plotted in the upper plot using different markers and colours depicting the different polarities. The migrating case has been plotted in the lower plot.

9.7 Doping Profile (4)

This scenario is the extreme doping scenario; these *V-I* curves and gain are to be compared to the non-migrating case depicted in figure 17 (a), profile (3). That is the reason why the nominal case has been plotted in pink in the *V-I* plot. The *V-I* plot for this study is different, see figure 22 (a). The pre-peaks are even weaker and the current density does not grow as high. Looking at the *V-I* plot from the positive bias, the lasing resonance is more broadened, and beyond the lasing peak the NDR is very low. Besides the current density continues to grow higher. At higher positive bias there is an indication of a resonance at 66 mV per period. This peak is also seen in the *V-I* plot in Ref. [10], see figure 15 (c), and it is very similar to the reference plots except that the current density does not grow as high and not all of the pre-peaks are present. This indicates that this doping structure lies closer to the doping migration than previous implementations. The NDR after the lasing peak is much lower compared to the previous case. This is due to that the constant doping density is lower and homogeneous throughout the doping layer. The number of scatterings per nm will be lower compared to the previous doping profile.

In figure 22 (b) it can be seen that the energy separation between the two photon energies is smaller than for the previous doping profile. The photon energy at negative bias is around 15 meV and the photon energy at positive bias is 17.5 meV. The gain does not grow as high as for the previous asymmetric doping profile. However now the gain is higher at the positive biases than the negative biases. In the previous investigation the gain was almost the same for both polarities. The *V-I*

results for this case is closer to the results presented in the reference, even though the energy separation between the different polarities is smaller but not as small as the 0.3 meV separation reported in ref [10].

Part III
Conclusion and Outlook

10 Conclusion

In this thesis the impact of changing the doping layers on the performance of three different QCL structures, [9, 10, 24], has been investigated. First the doping density and the doping position were changed on one or several of the QCL samples in order to see how the calculated I-V and gain change; see sections 7 and 8 for these results. Dopant migration effects were investigated on the symmetric QCL presented in reference [10], see section 9 for these results.

When increasing the doping density the I-V curve changes and the resonance peaks gets more broadened and the NDR becomes less pronounced. The photon energy and the gain increase with increasing doping density. These changes can to the largest extent be accounted to that the number of scattering events increases but also that the MF shifts. However this is very small compared to the effect of the scattering (see figures 10 (a)-(b)). Increased scattering leads to increased current but decreased tunnelling efficiency.

Changing the position of the doping layer, changes the behaviour of the I-V curves, the photon energies and the gain. Putting the doping layer in the barrier after the laser transition gives a much larger gain compared to the other barriers and wells. It is also beneficial to place two doping layers, one in the injector region and in the active region as this also gives a higher gain. This can be accounted to that the position where the scattering occurs changes and the MF changes.

The last part of this thesis concerns dopant migration effects. The effects of "soft" migration (see figure 17(b), profiles (1)-(3)) were small. The diffusion is probably larger and it was found that when the impurities are placed more or less homogeneously over a wider region the correspondence to the experimental results in [10] improved.

The model does not take the electron-electron scattering into account, so these results have to be taken with some reservation as the electron-electron scattering does affect the I-V characteristics and the gain experimentally. The electron-electron scattering should give a broadening of the I-V peaks and the pre-peaks might almost disappear. The electron-electron scattering will increase when increasing the doping density and this would heat the material. This would decrease the gain as gain decreases with increasing temperature. There will be a discrepancy as well between the theoretically calculated gain and what will be received experimentally as absorption increases with increasing doping density [11]. When absorption increases the optical output of the laser decreases.

11 Outlook

The worst case scenario, assuming that the diffusion reaches a equilibrium scenario of homogeneous doping should be simulated as well for the first profile of the migration study. It is indicated that this fits the experimental data better. The doping density study can be investigated further. As the electron-electron scattering is not part of the model, this can be estimated by changing the acoustical phonon frequency for instance on one of the higher doping densities used during this thesis. Also the results can be simulated in the future again when electron-electron scattering has been successfully added.

The density study can be taken further by simulating all the different doping cases without the MF and the scattering for a better at hand approach. Now this was done on one of the studies and even though it suggested that the interpretation was correct it is only one data point and several do provide a better basis. This could as wells be extended to the position study, as then it could be made visible if the resonance would change without the MF.

Part IV
Appendices

Appendix A

Table 1: Parameters that remain constant in two well laser [9].

Parameter	Value
x	0.15
Conduction band offset	127.5meV
Effective mass barriers	$7.945 \cdot 10^{-2}$
Effective mass wells	0.067
Λ	10
η	0.15
N_E	900
N_k	600
Number of Wannier - Stark states	6
Number of z-points	500
N_{per}	2
N_{nu}	5

Table 2: Parameters that remain constant in the asymmetric three well laser [24].

Parameter	Value
x	0.15
Conduction band offset	127.5 meV
Effective mass barriers	$7.945 \cdot 10^{-2}$
Effective mass wells	0.067
Λ	10
η	0.2
N_E	700
N_k	700
Number of Wannier - Stark states	8
Number of z-points	700
N_{per}	1
N_{nu}	8

Table 3: Parameters that remain constant in symmetric three well laser [10].

Parameter	Value
x	0.15
Conduction band offset	127.5meV
Effective mass barriers	$7.945 \cdot 10^{-2}$
Effective mass wells	0.067
Λ	10
η	0.15
N_E	900
N_k	600
Number of Wannier - Stark states	6
Numer of z-points	500
N_{per}	2
N_{nu}	5

Table 4: Bias per period at which gain was calculated at for the doping density study on [9].

Doping density unit $n_{2D,ref}$ cm^{-2}	n_{2D} cm^{-2}	Resonance mV per period
$\frac{1}{10}$	$1.5 \cdot 10^9$	46.1
$\frac{1}{2}$	$7.5 \cdot 10^9$	46.3
1	$1.5 \cdot 10^{10}$	47.3
2	$3.0 \cdot 10^{10}$	47
3	$4.5 \cdot 10^{10}$	47.4
4	$6.0 \cdot 10^{10}$	48
5	$7.5 \cdot 10^{10}$	49.9
7.5	$1.125 \cdot 10^{11}$	48
10	$1.5 \cdot 10^{11}$	51

Table 5: Table over doping layers for the two well laser [9] in the position study.

Position	Layer colour	z_{start} nm	z_{end} nm	n_{3D} cm $^{-3}$	n_δ
1	Red	0.9	2.9	7.5×10^{16}	3
2	Cyan	11.75	13.75	7.5×10^{16}	3
3	Green	22.95	24.95	7.5×10^{16}	3
4	Blue	29.35	31.35	7.5×10^{16}	3
5	Black slice 1	12.35	13.35	7.5×10^{16}	3
5	Black slice 2	29.85	30.85	7.5×10^{16}	3

Table 6: Table over doping layers for the asymmetric three well laser [24] in the position study.

Position	Layer colour	z_{start} nm	z_{end} nm	n_{3D} cm $^{-3}6n_{\delta}$	
1	Magenta	1.1	3.1	1.5×10^{17}	1
2	Cyan	11.40	13.40	1.5×10^{17}	1
3	Green	22.00	24.00	1.5×10^{17}	1
4	Blue	28.65	30.65	1.5×10^{17}	1
5	Red	34.30	36.30	1.5×10^{17}	1
6	Orange	39.95	41.95	1.5×10^{17}	1
7	Black slice 1	11.90	12.90	1.5×10^{17}	1
7	Black slice 2	29.15	30.15	1.5×10^{17}	1

Table 7: Bias per period at which each gain was calculated at in the position study of [9]

Position	Bias per period [mV]
1	45.6
2	47.3
3	45.6
4	40.6

Table 8: Bias per period at which each gain was calculated at in the position study of [24]

Position	Bias per period [mV]
0	58.7
1	62.7
2	52.7
3	48.5
4	50.6
5	56.5
6	54.0

Table 9: Table over nomial doping layers for the symmetric three well laser [10] in the migration study , see figure 17(a) profiles (1)-(3).

Position	Layer colour	z_{start} nm	z_{end} nm	n_{3D} cm $^{-3}$	n_{δ}
1	Red	0.00	16.40	2.0×10^{16}	3
2	Blue	0.00	7.90	4.15×10^{16}	3
3	Black slice 1	0.00	7.90	2.0×10^{16}	3
3	Black slice 2	32.20	40.20	2.0×10^{16}	3

Table 10: Table over doping layers for the symmetric three well laser [10] in migration study for case 1, see figure 17(b) profile (1).

Layer	z_{start} nm	z_{end} nm	n_{3D} cm $^{-3}$	n_δ
1	0.00	14.40	2.00000 $\times 10^{16}$	3
2	14.40	16.40	1.07640 $\times 10^{16}$	1
3	16.40	18.40	5.34370 $\times 10^{16}$	1
4	18.40	20.40	2.44710 $\times 10^{15}$	1
5	20.40	22.40	1.03376 $\times 10^{15}$	1
6	22.40	24. 40	4.02833$\times 10^{14}$	1

Table 11: Table over doping layers for the symmetric three well laser [10] in migration study for case 2 , see figure 17(b) profile (2).

Layer	z_{start} nm	z_{end} nm	n_{3D} cm $^{-3}$	n_δ
1	0.00	5.9	4.1519 $\times 10^{16}$	3
2	5.9	7.9	2.2862 $\times 10^{16}$	1
3	7.9	9.9	1.1206 $\times 10^{16}$	1
4	9.9	11.90	4.8899$\times 10^{15}$	1
5	11.90	13.90	1.7994 $\times 10^{15}$	1
6	13.90	15.90	6.5682$\times 10^{14}$	1

Table 12: Table over doping layers for the symmetric three well laser [10] in migration study for case 3 , see figure 17(b) profile (3).

Layer	z_{start} nm	z_{end} nm	n_{3D} cm $^{-3}$	n_δ
1	0.00	1.5	2.02 $\times 10^{16}$	1
2	1.5	5.9	2.00 $\times 10^{16}$	3
3	5.9	7.9	1.2 $\times 10^{16}$	1
4	7.9	9.90	5.00$\times 10^{15}$	1
5	9.90	11.90	2.5 $\times 10^{15}$	1
6	11.90	13.90	8.00$\times 10^{14}$	1
7	32.20	38.70	2.00 $\times 10^{16}$	3
8	38.70	40.70	1.20 $\times 10^{16}$	1
9	40.70	42.70	5.00 $\times 10^{15}$	1
10	42.70	44.70	2.5$\times 10^{15}$	1
11	44.70	45.20	6.0 $\times 10^{14}$	1

Table 13: Table over doping layers for the symmetric three well laser [10] in migration study for case 4, see figure 17(b) profile (4).

Layer	z_{start} nm	z_{end} nm	n_{3D} cm $^{-3}$	n_δ
Orange slice 1	0.00	3.50	2.022700 $\times 10^{16}$	1
Orange slice 2	3.50	15.9	1.012346 $\times 10^{16}$	3
Orange slice 3	32.20	45.20	1.012346 $\times 10^{16}$	3

Table 14: Bias per period at which each gain was calculated at in the position study and migration study of [10]

Position	Bias per period [mV]
(a) position (1)	-55 +55
(a) position (2)	-55 +55
(a) position (3)	-57 +57
(b) position (1)	-55 +55
(b) position (2)	-55 +55
(b) position (3)	-57 +55
(b) position (4)	-55 +56

Appendix B

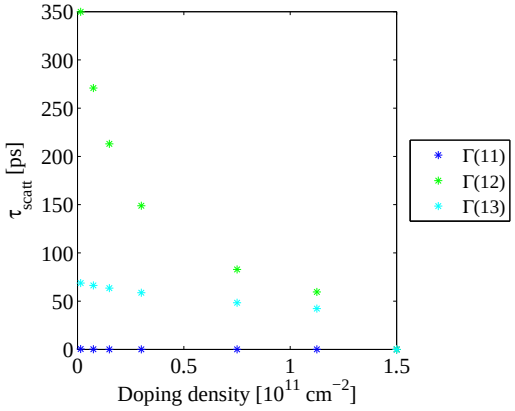

(a)

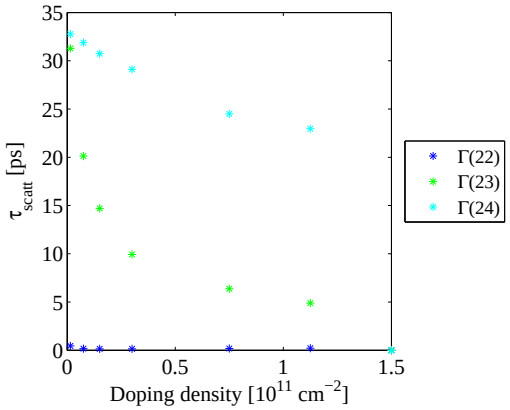

(b)

Figure 23: The scattering times between the states of the doping density study. 1 is the injector state, 2 is the LLS and 3 is the ULS. Scatterings to higher subbands are ignored.

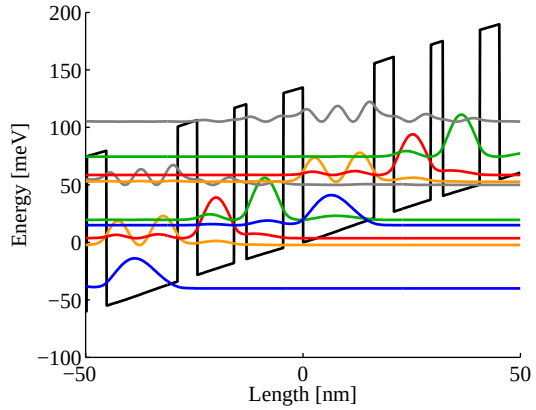

(a)

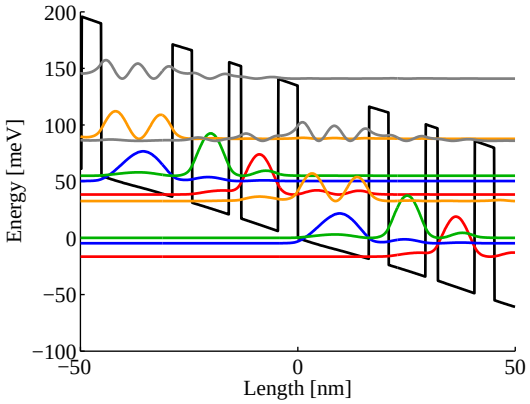

(b)

Figure 24: The Wannier - Stark states of the first asymmetric doping profile in migration study, before adding migratory effects. (a) At +55mV per period. (b) at -55mV per period.

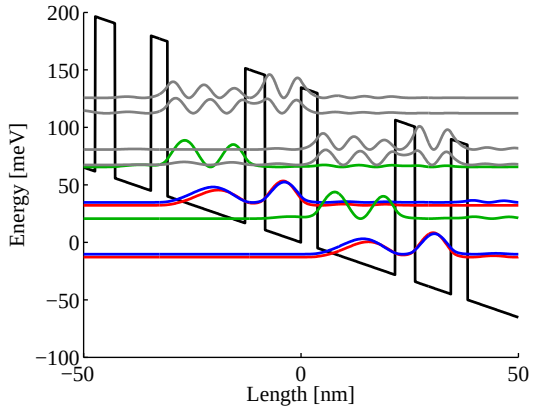

(a)

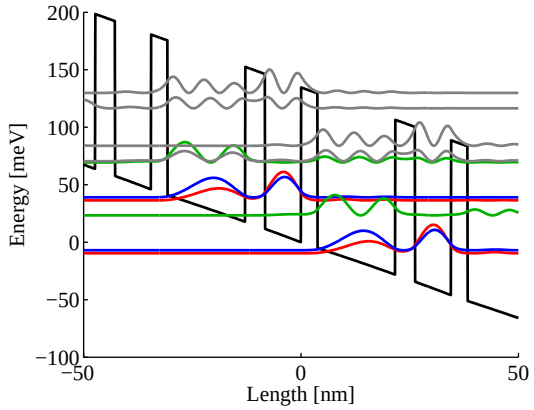

(b)

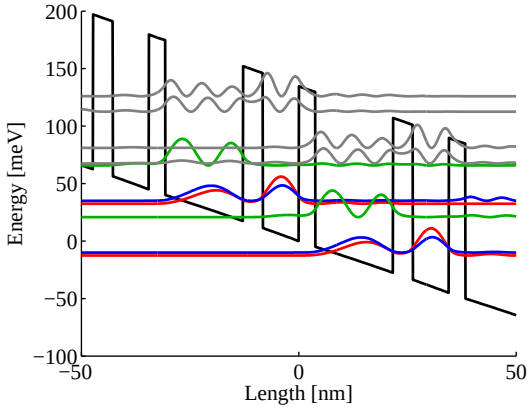

(c)

Figure 25: The Wannier - Stark states for position 1 (a)without mean-field (b) without impurity scattering (c) with both contributions. The state plotted in blue is the injector/extraction state, the state plotted in red is the ULS and green the LLS.

12 References

[1] J. Faist, F. Capasso, D.L. Sivco, C. Sirtori, H.A. L., A.Y. Cho, Science **264**, 553 (1994)

[2] A. Wacker, M. Lindskog, D.O. Winge, IEEE Journal of Selected Topics in Quantum Electronics **19**(5), 1200611 (2013)

[3] A. Wacker, in *Nonlinear laser dynamics*, ed. by K. Lüdge (Wiley - VCH, Weinheim, 2012), pp. 91–110

[4] M. Bugajski, P. Gutowski, P. Karbownik, A. Kolek, G. Hałdaś, K. Pierściński, D. Pierścińska, J. Kubacka-Traczyk, I. Sankowska, A. Trajnerowicz, K. Kosiel, A. Szerling, J. Grzonka, K. Kurzydłowski, T. Slight, W. Meredith, Physica Status Solidi (B) Basic Research. **251**(6), 1144 (2014)

[5] T.T. Lin, H. Hirayama, Phys. Status Solidi C **10**(11), 1430 (2013)

[6] J. Faist, *Quantum Cascade Lasers*, 1st edn. (Oxford University Press, Oxford, 2013)

[7] S.A. Holgate, *Understanding Solid State Physics* (CRC Press Taylor & Francis Group, 2010)

[8] E. Linfield, MBE growth of GaAs-AlGaAs terahertz frequency quantum cascade lasers (2014). IQCLW2014

[9] G. Scalari, M. Armanti, C. Walther, R. Terazzi, J. Faist, Optics Express **18**, 8043 (2010)

[10] C. Deutsch, H. Detz, M. Krall, M. Brandstetter, T. Zederbauer, A.M. Andrews, W. Schrenk, G. Strasser, K. Unterrainer, Applied Physics Letters **102**(20), 201102 (2013)

[11] A. Kolek, G. Hada, M. Bugajski, K. Pierściński, P. Gutowski, IEEE Journal of Selected Topics in Quantum Electronics. **21**(1), 1200110 (2015)

[12] D. Winge, Nonlinear Response of a Quantum Cascade Laser in a High Intensity Electromagnetic Field. Master's thesis, Lund University (2012). Available on LUP Student Papers

[13] M. Lindskog, Analysis and Optimisation of Quantum Cascade Structures. Master's thesis, Lund University (2012). Available on LUP Student Papers

[14] C. Kittel, *Introduction to Solid State Physics*, eigth edn. (John Wiley & Sons, USA, 2005)

[15] A. Wacker, Notes for solid state theory fff051/fyst25 (2012)

[16] M. Glück, A. Kolovsky, H.J. Korsch, N. Moiseyev, The European Physical Journal D **4**, 239 (1998)

[17] A. Wacker, *ProgrammPaket NEGF* (2011). Internal use only

[18] P. Hofmann, *Solid State Physics: An Introduction* (WILEY-VCH Verlag GmbH & Co. KGaA, Weinhem, 2008)

[19] A. Ferreira, G. Bastard, Phys. Rev. B. **40**(2), 1074 (1989)

[20] C. Jirauschek, T. Kubis, Applied Physics Reviews **1**(1), 011307 (2014)

[21] H. Haug, A.P. Jauho, *Quantum Kinetics in Transport and Optics of Semiconductors*, 1st edn. (Springer-Verlag Berlin Heidelberg, 1996)

[22] H. Bruus, K. Flensberg, *Many-body quantum theory in condensed matter* (Oxford University Press, Oxford, 2004)

[23] G.D. Mahan, *Many-Particle Physics*, 2nd edn. (Plenum Press, New York, 1990)

[24] S. Kumar, Q. Hu, J.L. Reno, Applied Physics Letters **94**(13), 131105 (2009)

[25] A. Benz, G. Fasching, A.M. Andrews, M. Martl, K. Unterrainer, T. Roch, W. Schrenk, S. Golka, G. Strasser, Applied Physics Letters **90**(10), 101107 (2007)

[26] H.C. Liu, M. Wächter, D. Ban, Z.R. Wasilewski, M. Buchanan, G.C. Aers, J.C. Cao, S.L. Feng, B.S. Williams, Q. Hu, Applied Physics Letters **87**(14), 141102 (2005)